TITLE PAGE

ENGINEERING DEVELOPMENT OF SLURRY BUBBLE COLUMN REACTOR (SBCR) TECHNOLOGY

Quarterly Technical Progress Report No. 23
For the Period 1 October – 31 December 2000

FINAL

Prepared by
AIR PRODUCTS AND CHEMICALS, INC.
7201 Hamilton Blvd.
Allentown, PA 18195-1501

Bernard A. Toseland, Ph.D.
Program Manager and Principal Investigator

Robert M. Kornosky
Contracting Officer's Representative

For the United States Department of Energy
Under Cooperative Agreement No. DE-FC22-95PC95051
Performance Period 3 April 1995 – 31 March 2002

DISCLAIMER

Comprehensive Table of Contents

ENGINEERING DEVELOPMENT OF SLURRY BUBBLE COLUMN REACTOR (SBCR) TECHNOLOGY

Quarterly Technical Progress Report No. 23

For the Period 1 October – 31 December 2000

Project Objectives

The major technical objectives of this program are threefold: 1) to develop the design tools and a fundamental understanding of the fluid dynamics of a slurry bubble column reactor to maximize reactor productivity, 2) to develop the mathematical reactor design models and gain an understanding of the hydrodynamic fundamentals under industrially relevant process conditions, and 3) to develop an understanding of the hydrodynamics and their interaction with the chemistries occurring in the bubble column reactor. Successful completion of these objectives will permit more efficient usage of the reactor column and tighter design criteria, increase overall reactor efficiency, and ensure a design that leads to stable reactor behavior when scaling up to large-diameter reactors.

Abstract

Washington University's work during the reporting period involved the implementation of the automated calibration device, which will provide an advanced method of determining liquid and slurry velocities at high pressures. This new calibration device is intended to replace the original calibration setup, which depended on fishing lines and hooks to position the radioactive particle. The report submitted by Washington University contains a complete description of the new calibration device and its operation. Improvements to the calibration program are also discussed. Iowa State University utilized air-water bubble column simulations in an effort to determine the domain size needed to represent all of the flow scales in a gas-liquid column at a high superficial velocity. Ohio State's report summarizes conclusions drawn from the completion of gas injection phenomena studies, specifically with respect to the characteristics of bubbling-jetting at submerged single orifices in liquid-solid suspensions.

Executive Summary

Washington University's newly developed automated calibration device is described in this quarter's report, and its theory of operation is explained. With the commissioning of the new calibration equipment, the Washington University group was prepared for high-pressure CARPT experiments. Successful testing of the equipment confirmed this. Stepper motors have been added to the calibration device to provide the most accurate positioning of the tracer particle. A C++ program has been developed to control the movement of the calibration device and has been incorporated in the principal calibration program. A new robust and accurate tracer reconstruction approach has been developed based on a better understanding and modeling of the physics behind the photon emission phenomenon. A new tracer data acquisition strategy has been implemented that contains the spread in the calibration curve in a stainless steel column. This new strategy enables the usage of the existing spline-based reconstruction method to provide reasonable estimates of the tracer location in a stainless steel column.

Iowa State's work for the quarter began with a set of simulations, which were divided on the bases of grid and domain sizes. All earlier simulations depended upon the sequential version of CFDLIB code. The parallel version of this code, which has been put into practice, has limitations, however. Consultants have begun work with the Iowa State team to resolve the problem. As a means of preparation for an Alpha cluster machine, scaleup studies of the Ames Laboratory Intel cluster were performed for three-dimensional simulations.

Ohio State reported the completion of the study of high-pressure gas injection from a single orifice submerged in a liquid-solid suspension. The Ohio State research group found that there is a decrease in bubbling-jetting transition velocity with increases in pressure and velocity when particles are present. Ohio State also reported on its studies of axial liquid-phase mixing, beginning with a review of the significant literature on the subject.

WASHINGTON UNIVERSITY IN ST. LOUIS

The report for Washington University for the period follows.

ENGINEERING DEVELOPMENT OF
SLURRY BUBBLE COLUMN REACTOR (SBCR) TECHNOLOGY

Twenty-third Quarterly Report
for
October 1 - December 31, 2000

(Budget Year 6: October 1, 2000 – September 30, 2001)

Chemical Reaction Engineering Laboratory
Chemical Engineering Department
Washington University

Objectives for the Sixth Budget Year

The main goal of this subcontract is to study the fluid dynamics of slurry bubble columns and address issues related to scaleup and design. The objectives set for the sixth budget year (October 1, 2000, – September 30, 2001) are listed below.

- Extension of the CARPT database to high superficial gas velocity in bubble columns.
- Extension of the CARPT/CT database to gas-liquid-solid systems at high superficial gas velocity.
- Evaluation of the effect of sparger design on fluid dynamics in bubble columns using the CARPT technique.
- Interpretation of LaPorte tracer data.
- Further improvement in Computational Fluid Dynamics (CFD) using CFDLIB and Fluent.

In this report, the research progress and achievements accomplished in the twenty-third quarter (October 1 – December 31, 2000) are summarized.

Highlights for the Twenty-Third Quarter

Implementation of Automated Calibration Device

- High-pressure CARPT calibration device has been designed and constructed.
- Successful testing has been performed at high pressure.
- Stepper motors have been added to the calibration device to provide the most accurate positioning of the tracer particle.
- A C++ program has been developed to control the movement of the calibration device and has been incorporated in the principal calibration program.

Evaluation of Tracer Position Reconstruction Strategies in the High-Pressure Bubble Column Reactor (HPBCR)

- A new robust and accurate tracer reconstruction approach has been developed based on a better understanding and modeling of the physics behind the photon emission phenomenon.

A New Data Acquisition Strategy

- A new tracer data acquisition strategy has been implemented that contains the spread in the calibration curve in a stainless steel column. This new data acquisition strategy enables the usage of the existing spline-based reconstruction method to provide reasonable estimates of the tracer location in a stainless steel column.

1. IMPLEMENTATION OF AUTOMATED CALIBRATION DEVICE

To determine the liquid and slurry velocity measurements at high pressure by the Computer Automated Radioactive Particle Tracking (CARPT) technique, all the detectors first must be calibrated at the operating conditions of interest. This calibration is accomplished by positioning the radioactive source and recording the radioactivity readings at all the detectors.

The high-pressure slurry bubble column reactor is made of stainless steel. The earlier method of calibration, which relied on fishing lines and hooks to position the radioactive particle, does not work because the column is not transparent and the system must be kept closed to maintain the high pressure. Hence, a different calibration device has been designed, constructed and successfully tested to accomplish the calibration in-situ at high pressure.

1.1 Design and Fabrication of the Device

The setup for the high-pressure bubble column is designed to handle a high airflow rate at a pressure of 200 psig. The stainless steel column of 6.3-in. diameter has a wall thickness of 3 mm. This thickness has been optimized to reduce the activity of the radioactive tracer particle. In addition, to avoid the radioactive beam attenuation due to wall thickness variation, the column is equipped with a minimum number of ports for pressure gauges, for liquid drainage and for checking overflow level via a small window. This column has been designed only for CAPRT/CT experiments. Another identical column for flow visualization and more intrusive probing of the flow patterns has already been designed and constructed and is equipped with several ports and transparent windows along the column. Figure 1.1 shows the CARPT setup with the stainless steel column. The detectors around the column have been accurately fixed at known positions with a Laser pointer.

The calibration with fishing lines and hooks is impossible in this opaque system, particularly in the high-pressure bubble column. The first version of the new calibration device was designed and constructed in CREL, as shown in Figure 1.2. This device is mounted at the top-flange of the column with a paper gasket and eight screws. It is equipped with a hand wheel for adjusting the axial level of the tracer particle via the vertical ruler and with a horizontal bar for controlling the angular motion of the tracer particle by 5^{o} increments. The device is equipped with hydraulic seals that can sustain pressures up to 1000 psig, as shown in Figure 1.3.

The detailed configuration of this calibration device is presented in Figure 1.2, which shows the external parts of the device, and in Figure 1.3, which illustrates the internal parts. The device consists of the following parts:

1. **Spider Support:** The spider-like support that carries the rod on which the radioactive tracer is mounted is made of three 3/8-in. diameter tubes (referred to as part number 1 in Figure 1.3). A ball is fixed at the end of each of the three tubes. The balls rotate in any direction to ensure that the support can move up and down and also rotate in the azimuthal direction. Attached to the balls are springs, which are under tension, always pushing the support-structure tubes against the column wall, so that the whole device is

supported rigidly. The springs also provide for a smooth azimuthal movement. The balls are of the same size and the springs have the same tension. The whole structure is fixed to two rigid ¾-in. diameter suspension rods (part 2 in Figure 1.3) with a length of about 14 in. These two rigid rods ensure that the whole device moves vertically without any bending and rotates without distortion. The particle-holding rod (part 3) has two sections. The upper section is made of stainless steel material, which is firmly fixed at the particle-holding base (part 4) with a screw. The lower section, where the radioactive tracer is fixed, is made of aluminum to reduce γ ray attenuation. The whole support and the particle-holding rod are designed to prevent the rod from vibrating when there is a turbulent flow in the column.

2. **Base for holding particle:** The base (part 4) is welded at the center below the spider. Special care has been taken to ensure perfect horizontality of the particle-holding base arm. This arm is absolutely perpendicular to the column wall. The arm of the particle-base has a number of specially machined guides for insertion of the particle-holding rod. Precise machining ensures that the particle-holding rod can be mounted at seven different radial locations, all parallel to the column wall.
3. **Suspension rods:** The suspension rods (part # 2 in Figure 1.3) are made of six pairs of stainless steel tubing of ¾-in. diameter and 14-in. length (which are connected with screws). This allows the extension of the structure to reach the bottom of the column. The suspension rods are made in six pieces because of the limited headspace at the top of the column. Scales for axial and angular divisions are engraved on the calibration device.
4. **Hydraulic seals:** The hydraulic seals of the suspension rods are tight enough to prevent the system from dripping when other suspension rods are introduced. This eliminates the need for locking the rods while adding to the structure.

The calibration device has been fabricated for the 6.3-in. diameter column to be used at atmospheric or elevated pressure. This device can be readily used for different column diameters with minor modifications.

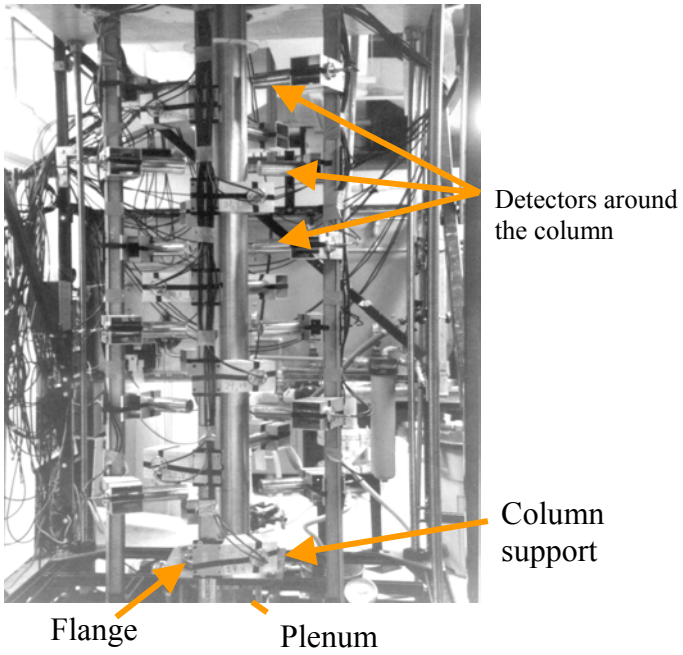

Figure 1.1 CARPT Setup for the High-Pressure Bubble Column

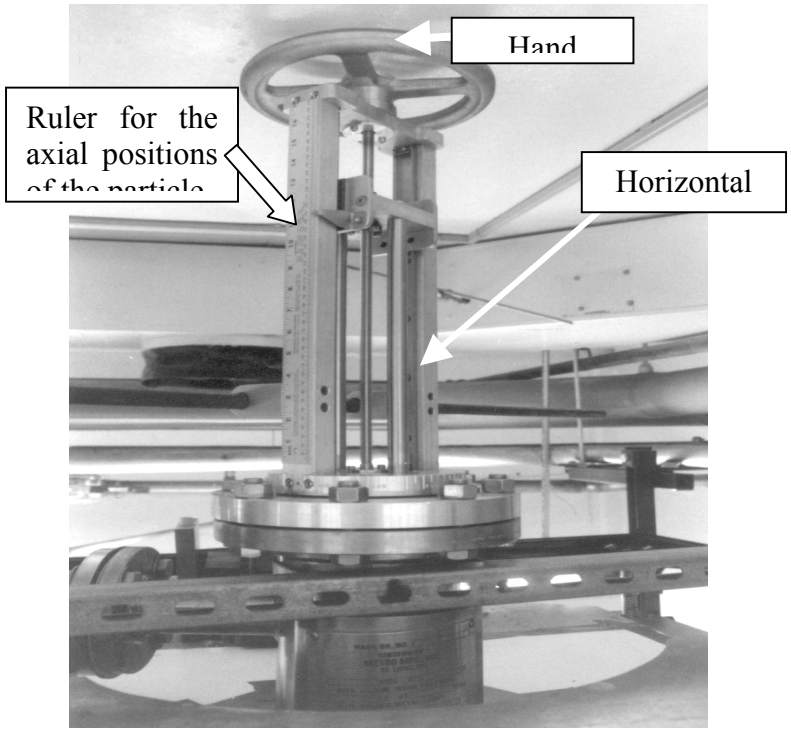

Figure 1.2 Calibration Device Mounted at the Top Flange of the Stainless Steel Column

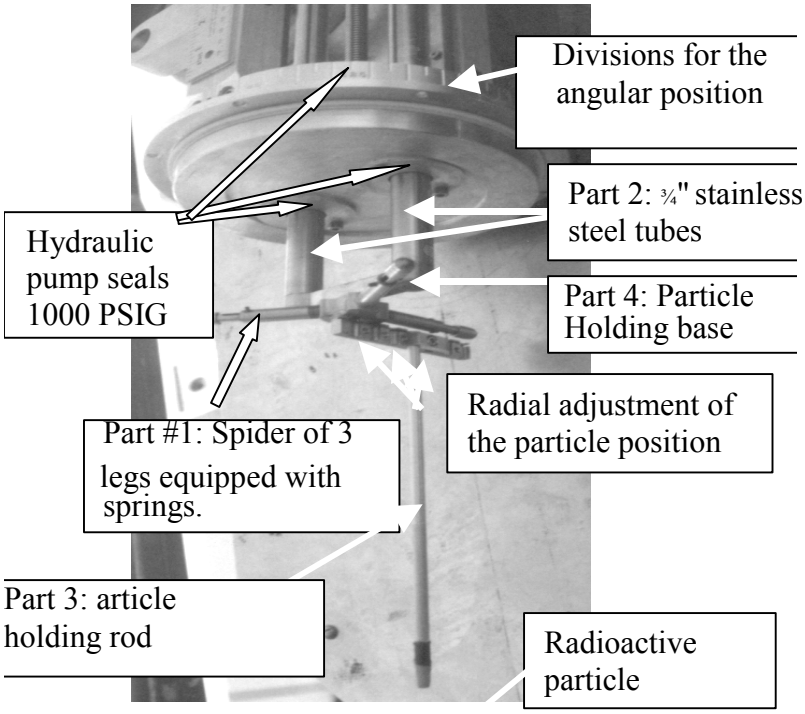

Figure 1.3 Parts Constituting the Calibration Device

1.2 Device Testing

The above-described calibration device has been used to perform the test calibration by acquiring signals from 2000 points in the column at a pressure of 3 atmospheres. The results were encouraging as no leak was observed, but considerable effort was required to move the particle in the azimuthal and axial directions. About 2 days were needed to perform this calibration. The calibration curves look similar to the ones obtained in bubble columns with the old calibration method (for example, Figure 1.4).

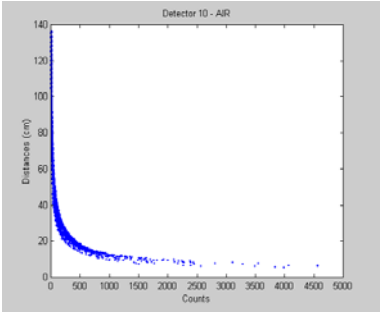

Figure 1.4 Calibration Curve Counts *vs* Distances for Detector 10

The calibration device was also tested at 7 atmospheres, and no leak was observed. To improve the ease of calibration at elevated pressures, stepper motors were added to the calibration device. This addition makes the calibration more accurate and eliminates the need to move the device manually. Figure 1.5 shows the modified final version of the

calibration device when the stepper motors are added, one powerful motor for the angular movement (shown in Figure 1.5 by the large size motor) and another motor replacing the hand wheel for the axial movement. A sophisticated program has been developed in C++ to control the angular and axial movement of the calibration device. This program has been carefully inserted in the principal calibration program as a subroutine. It should be pointed out that the radial position of the tracer must still be changed manually by fixing the tracer support rod at different radial positions. The performance of this automated calibration device is excellent; about 4000 calibration data points were acquired in the stainless steel column within a record time of 8 to 10 hours. The path is now paved for CARPT experiments at elevated pressure.

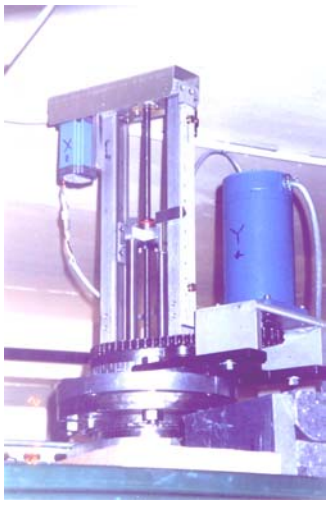

Figure 1.5 Automatic Calibration Device

2. EVALUATION OF TRACER POSITION RECONSTRUCTION STRATEGIES IN THE HIGH-PRESSURE BUBBLE COLUMN REACTOR (HPBCR)

2.1 Problem Definition

The first step in a CARPT experiment is to obtain a calibration map of the count registered by each detector for several hundred known locations of the tracer. A typical calibration curve obtained in a Plexiglas column is shown in Figure 2.1.

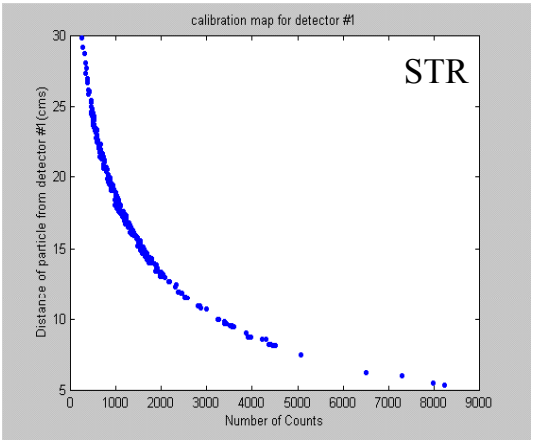

Figure 2.1 Calibration Map Obtained in a Plexiglas Stirred Tank Reactor

From Figure 2.1 it is clear that each count registered by a detector is associated with a unique distance of the tracer from that detector. For instance if detector #1 registers 3000 counts, then the tracer particle is 10.0 cm from detector #1. Hence this calibration curve can be expected to provide an accurate reconstruction of the distance of the tracer from each detector, which can then be used to obtain the exact tracer co-ordinates by solving a system of linear equations (Devanathan, 1991). However, when calibration experiments were performed in air in the stainless steel column, the calibration curve obtained looked very different, as shown in Figure 2.2.

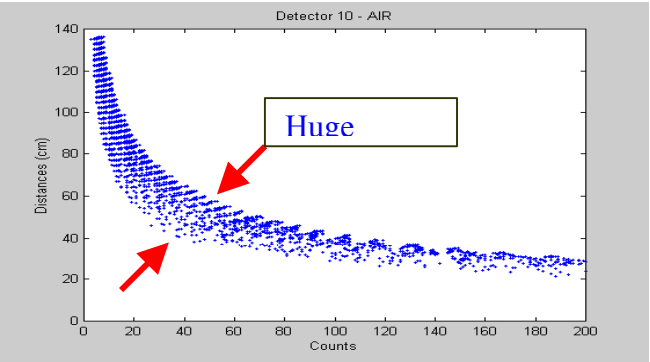

Figure 2.2 Calibration Map Obtained in the Stainless Steel Reactor

The calibration curve obtained in the stainless steel column shows a huge spread. With a curve of this form, the conventional approach of generating a spline of the form

$$d_{10} = f_{10}(C_{10}) - \quad - \quad -(2.1)$$

where d_{10} is the tracer distance from detector 10 and C_{10} is the count recorded at detector 10, will not work well, because if we feed a count of 100 (C_{10}) to equation (2.1), then the predicted distance d_{10} is 36 cm, while Figure 2.2 suggests that the distance of the tracer from detector 10, d_{10}, can be anywhere between 30-42 cm. This clearly indicates that the spline-based approach to fitting the count vs the distance data of Figure 2.2 would result in a considerable error in estimating the distances accurately. Further, it has been observed that even small errors in the reconstructed distances (~1-2mm) can be amplified considerably when solving for the exact tracer co-ordinates using the weighted least-squares regression technique (Devanathan, 1991). Hence, for systems in which the calibration curve looks like that shown in Figure 2.2, the existing approach cannot be used to reconstruct even the known calibration points, as illustrated clearly by Figure 2.3.

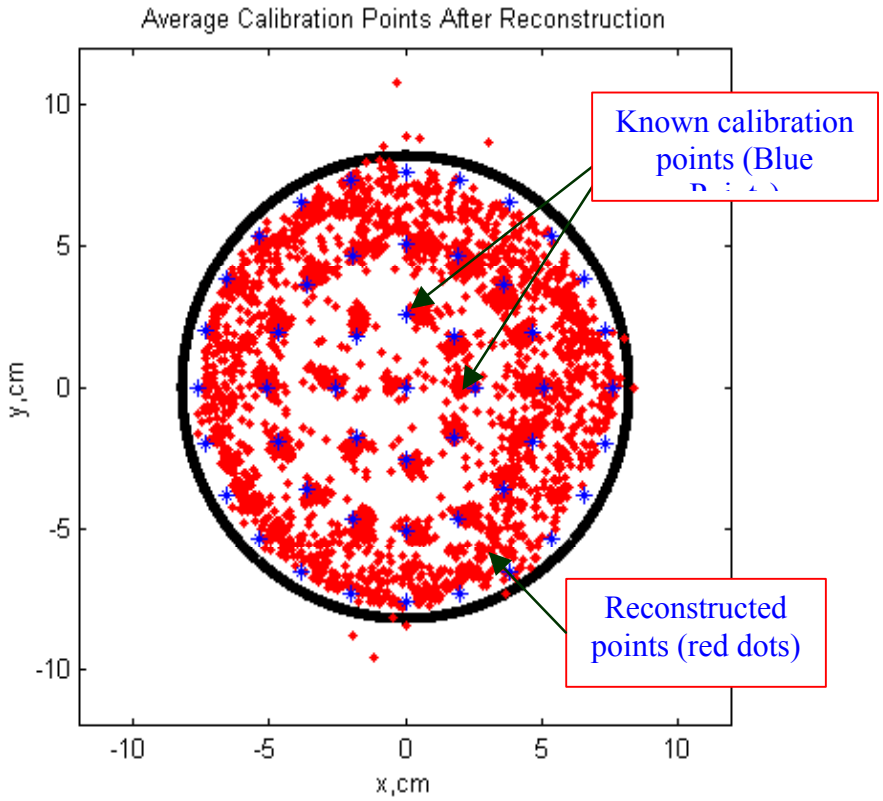

Figure 2.3 Reconstruction of 3528 Known Calibration Points

Figure 2.3 is a comparison between the actual calibration points shown by the blue points (3528 in all, corresponding to 49 points per axial plane and around 72 axial planes) and the reconstructed points (the red dots). Ideally the red dots should have fallen directly on top of the blue dots (implying exact reconstruction of calibration points). The spread of the red dots around each blue dot corresponds to the reconstructed location at each axial plane. This clearly illustrates that the existing spline-based reconstruction approach cannot be used to reconstruct even the known calibration points. As expected, the errors in reconstructing other tracer locations are larger, as shown in Figure 2.4.

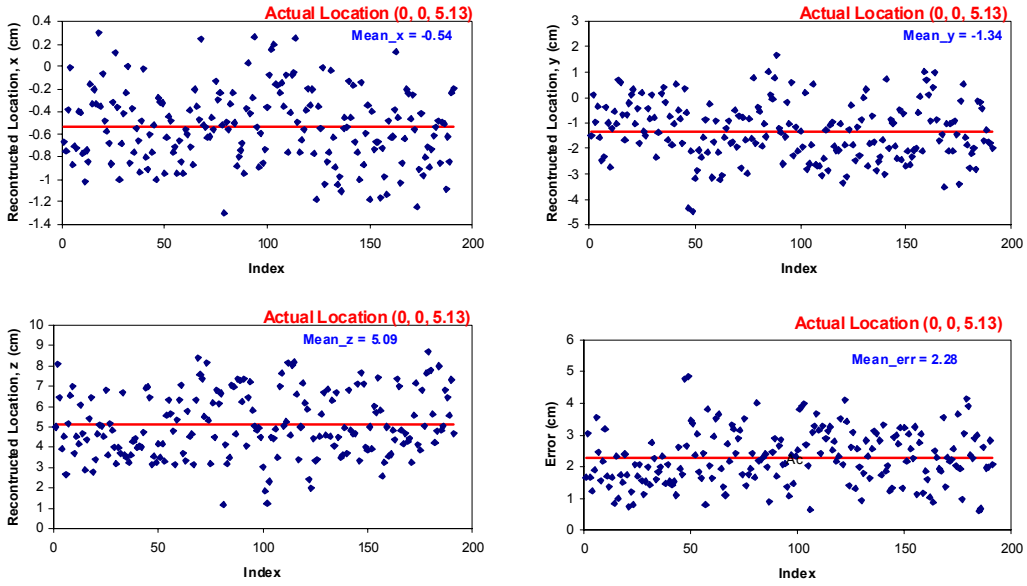

Figure 2.4 Reconstruction of Unknown Test Points Located at (r = 0 cm, θ = 0°, z = 5.13 cm)

Hence, the problem was identified to be the use of the existing spline-based reconstruction approach for systems whose calibration curve looks like that shown in Figure 2.2, and the further amplification of this error by use of the existing weighted least squares regression technique in identifying the exact tracer co-ordinates (x,y,z).

To remedy this situation, a two-pronged approach has been adopted in which i) the spline-based reconstruction and the weighted least squares regression are replaced by different approaches and ii) a new data acquisition strategy is outlined that confines the spread in the calibration curve, thus allowing the use of the existing reconstruction algorithms. Both are expected to provide better reconstruction of the calibration, as well as the unknown test points. The two new tracer position reconstruction approaches are outlined below, and in a separate follow-up section the new data acquisition protocol is discussed and illustrated.

2.2 New Reconstruction Approaches

2.2.1 A Look-Up Table Approach

Larachi et. al. (1994) used a two-step approach to reconstruct the unknown tracer position. In the first step they used the calibration data spread on a coarse grid (using only a few hundred calibration data) to generate the system constants such as detector dead times (τ_d), detector gains (R) and attenuation coefficients of the medium (μ_l, μ_g, etc.). They used these constants in a model that then generated an estimate of the counts for any particular position of the tracer with respect to a selected detector given by

$$C_{est} = \frac{T\nu R\phi\varepsilon}{1+\tau\nu R\phi\varepsilon} - \quad - \quad -(2.2)$$

where T is the sampling period (sec), ν is the number of γ ray photons emitted per disintegration of Sc^{46} (ν =2), ϕ is the photopeak efficiency and ε is the total intrinsic detection efficiency of the detector. The notations used are exactly the same as in Larachi et. al. (1994). This model was then used to generate a finer grid of calibration data that was then stored in the form of a lookup table. This is schematically outlined in Figure 2.5.

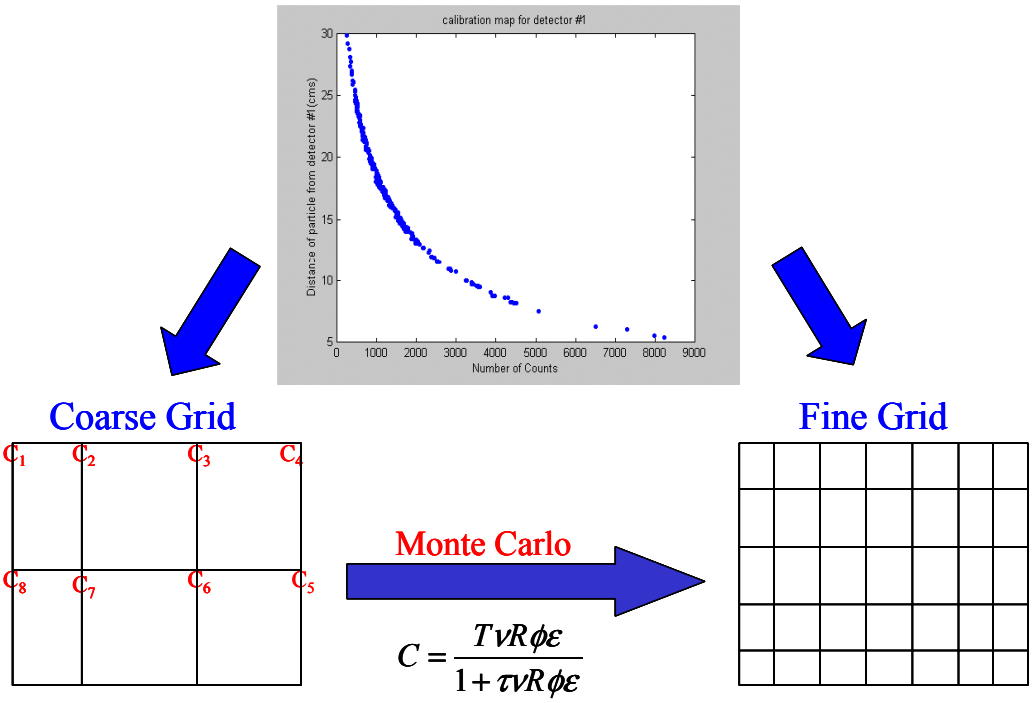

Figure 2.5 Generation of a Fine Grid of Calibration Data Either by Monte Carlo Simulations or Through Experiments

This first step of the Larachi et. al. (1994) procedure is redundant when calibration experiments have been performed on a dense grid as in the stainless steel reactor (3,528 points). Hence the calibration data can be organized directly into a lookup table, as shown in Figure 2.6.

X	Y	Z	C_1	C_2	C_3	C_4	C_5	C_6	C_7	C_8	C_9	C_{10}	C_{11}	C_{12}	C_{13}	C_{14}	C_{15}	C_{16}
0	0	0	396	420	12	37	45	89	120	5	56	71	80	110	92	370	41	4
0	0.2	0	--	---	---	---	---	---	---									
..	..																	..

Figure 2.6 Calibration Information Organized as a Lookup Table

The lookup table stores the co-ordinates of each calibration point and the corresponding time-averaged count registered by each detector. To reconstruct an unknown tracer location,

a quantity called the chi squared (χ^2) is computed at each node. The χ^2 is defined as follows:

$$\chi^2(j) = \sum_{i=1}^{N_D=16} \frac{(C_i - M_i)^2}{\sigma_i^2} - \quad - \quad -(2.3)$$

where j is the j^{th} calibration node, C_i is the count registered by the i^{th} detector at the j^{th} node (obtained from the lookup table), M_i is the count measured by the i^{th} detector when the particle is kept at an unknown location and $\sigma_i^2=C_i$. This χ^2 is computed for all the known calibration points (i.e., j=1 to 3528). The node that minimizes the χ^2 is identified as the node closest to the unknown point. The time-averaged counts corresponding to the known calibration points in the HPBCR are then fed into this algorithm. The algorithm yields perfect reconstruction of the calibration points, as shown in Figure 2.7.

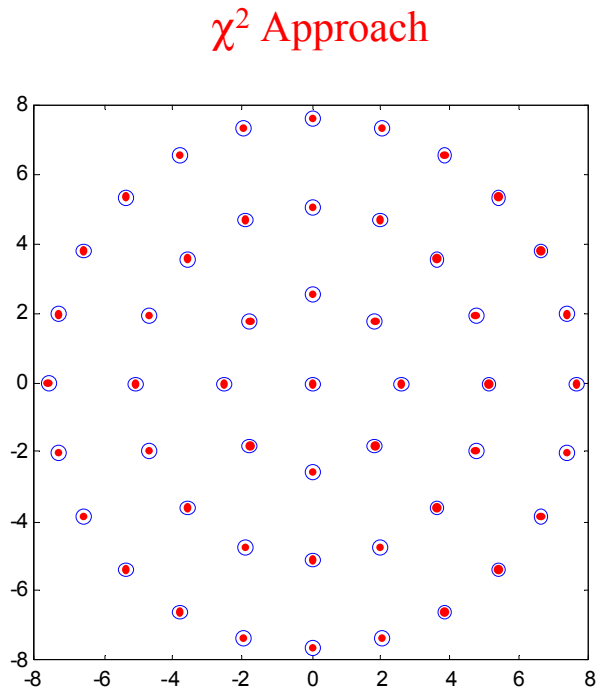

Figure 2.7 Reconstruction of 3,528 Known Calibration Points

This new algorithm, which does not use the spline-fitting/weighted least regression technique, clearly does an excellent job of reconstructing the known calibration points. Now the performance of this algorithm in reconstructing the unknown tracer location has to be evaluated. With the new algorithm, exact reconstruction is possible (as seen from Figure 2.7), provided the unknown point lies on the calibration nodes. However, if the unknown point lies in between the nodes, then the algorithm in its existing form cannot be expected to do a good job of reconstructing the unknown tracer location unless the calibration grid is extremely fine (Δx, Δy, Δz~0.05-0.1 mm). Hence, a second iteration has to be performed to identify the exact location of the unknown point. This is done by following the ideas

outlined in Larachi et. al. (1994). They generate a fine grid around the closest node identified in the first iteration, as shown in Figure 2.8.

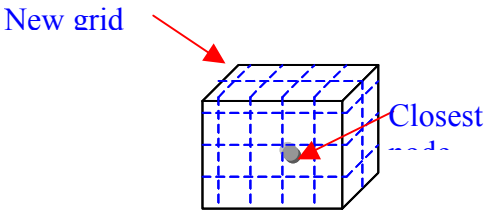

Figure 2.8 Generation of a Fine Mesh Around Closest Node

The new grid can be generated by an approximate formula given below:

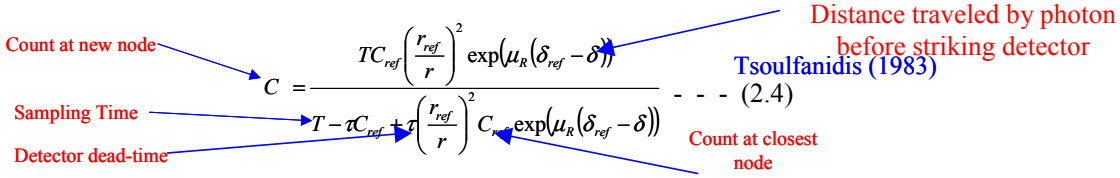

$$C = \frac{TC_{ref}\left(\frac{r_{ref}}{r}\right)^2 \exp\left(\mu_R(\delta_{ref}-\delta)\right)}{T - \tau C_{ref} + \tau\left(\frac{r_{ref}}{r}\right)^2 C_{ref}\exp\left(\mu_R(\delta_{ref}-\delta)\right)} \quad - - - \quad (2.4)$$

The information corresponding to the new grid is organized as a lookup table similar to Figure 2.6. The same criterion of χ^2 is then used to identify the exact location of the unknown test location. The formula in Equation (2.4) permits evaluation of the contribution of different physical phenomena like the effect of detector response time (τ_d), attenuation coefficient of the medium and attenuation coefficient of the stainless steel wall (μ_R). Three different approximations of (2.4) were used to evaluate the contribution of the different physical phenomena. The first model (M_1) ignored the attenuation coefficients and the detector dead times (i.e., μ_R and τ_d were set to zero), the second model (M_2) ignored the attenuation coefficient of the medium and the third model was the full model (M_3). The ability of M_1 and M_3 to reconstruct ten unknown test points is presented in Table 2.1.

Model	M_1	M_3	M_1	M_3
S.N.	σ_r (cm)	σ_r (cm)	σ_z (cm)	σ_z (cm)
1	0.64	0.55	0.31	0.20
2	0.78	0.67	0.20	0.06
3	0.74	0.77	0.40	0.31
4	0.72	0.66	0.21	0.09
5	0.56	0.61	0.16	0.11
6	0.57	0.69	0.18	0.06
7	0.60	0.59	0.26	0.12
8	0.66	0.59	0.18	0.18
9	0.77	0.60	0.25	0.20
10	0.57	0.61	0.18	0.18

Table 2.1 Reconstruction Accuracy of Ten Test Points using Model M_1 and M_3

From Table 2.1 it is clear that the model that accounts for the attenuation coefficient of the column wall is more accurate than model M_1, which ignores μ_R. The comparisons also suggest that while there are clear improvements in the accuracy of the axial co-ordinate reconstruction, not much improvement is seen in the reconstruction of the radial co-ordinate. The poorer resolution in the radial co-ordinate has little to do with the stainless steel column wall, and instead may be due to the presence of only two detectors at each axial plane (Roy et. al., 1999). The radial co-ordinate reconstruction worsened when only one detector per axial plane was used for the reconstruction, which confirms this assertion. Calculations also revealed that attenuation caused by the presence of the stainless steel column wall was sometimes as high as that encountered by a photon beam traveling ten times the distance in water (i.e., $\delta_{ss}=10\delta_{water}$). A comparison of the errors using M_3 in reconstruction indicates that the mean errors are much lower than the mean errors seen in Figure 2.4. Thus, it can be concluded that the new approach yields a definite improvement in reconstruction of the calibration points, as well as the unknown tracer locations.

2.2.2 Full Monte Carlo Approach

The comparisons between the three different models M_1, M_2 and M_3 suggested that modeling the "physics" of the different phenomena may improve the reconstruction accuracy. Hence, a full Monte Carlo model was developed in which the first step is similar to Larachi et. al. (1994), i.e., a Monte Carlo simulation is done to obtain calibration data on a finer grid (refer to Figure 2.9). However, a full Monte Carlo simulation with the HPBCR calibration data revealed that counts predicted by Monte Carlo simulations are often higher than the measured counts, as shown below in Figure 2.9. The overall percentage deviation with respect to the 45^o parity line was found to be positive, indicating that Monte Carlo overestimates the actual counts.

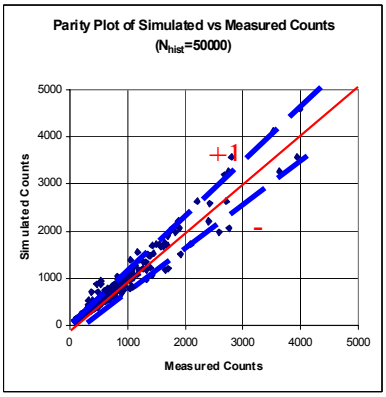

Figure 2.9 Comparison between Measured and Simulated Counts

This indicates that the presence of the "stainless steel" wall is causing the phenomenon of buildup to occur (Tsoulfanidis, 1983). Equation (2.2), used to generate a Monte Carlo estimate of the count, does not account for the phenomenon of buildup, which might explain the observed over-prediction in counts. Hence, a Monte Carlo simulation done with data containing the full energy spectrum will need to account for the phenomenon of buildup, which is not a trivial matter. The presence of buildup was confirmed by comparing the spectrum measured with and without stainless steel wall (Figures 2.10a and 2.10b).

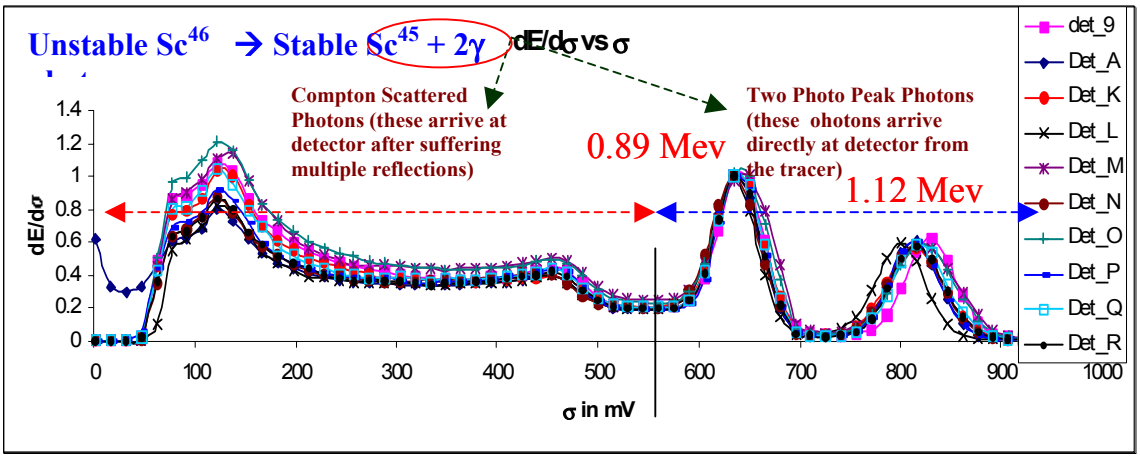

Figure 2.10a Photo Energy Spectrum Obtained in a Plexiglas Column

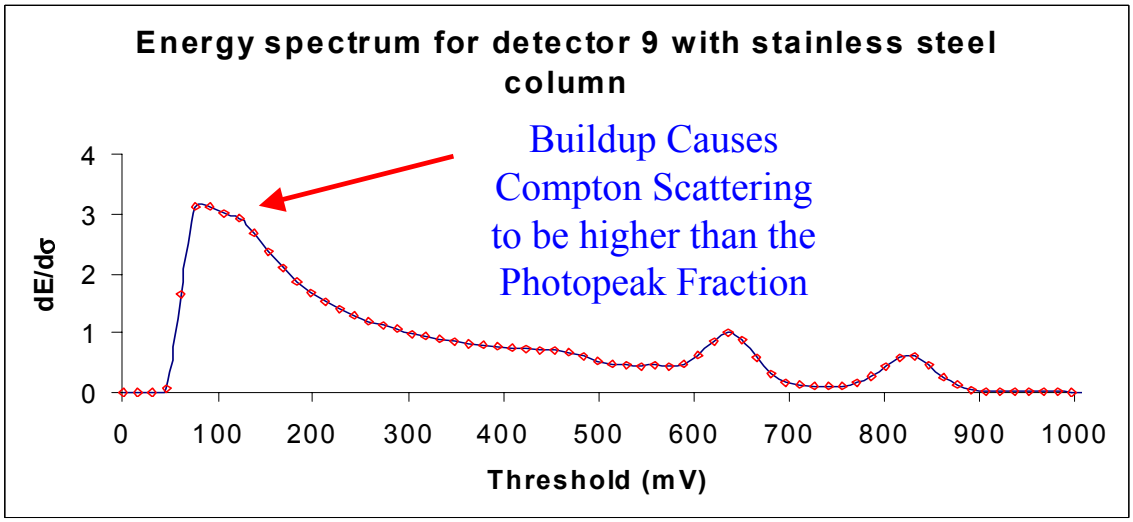

Figure 2.10b Photo Energy Spectrum Obtained in a Stainless Steel Reactor

Some preliminary attempts were made to model the phenomenon of buildup by developing an iterative neural network-based algorithm. The iterative scheme was not robust and did not yield converged results for the buildup function. Hence this approach was not further pursued. The only way to avoid modeling buildup is to constrain the detectors to acquire only the photopeak fraction of the photon energy spectrum. This means that the detectors should be constrained to collect only those photons with energy greater than 600mv (see Figures 2.10a and 21.0b). Then one can be certain that the data will not be corrupted by the buildup phenomenon. Some preliminary Monte Carlo simulations were done by acquiring data with a threshold of 560mV to register only the photopeak fraction. Monte Carlo simulations were carried out with 1000 photon histories. A fine grid of calibration data was generated using Monte Carlo simulations. The parity plots of the simulated vs measured

counts for the new data set are shown in Figure 2.11, which reveals improvement compared to Figure 2.9.

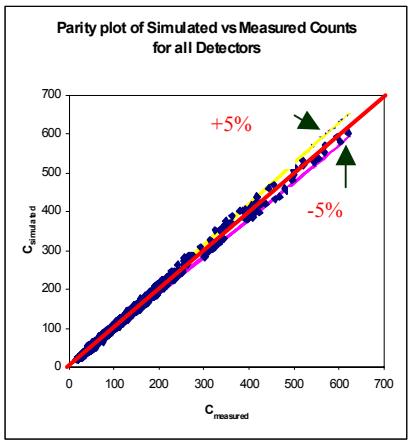

Figure 2.11 Comparison Between Measured and Simulated Counts

The parity plots indicate that simulated counts compare well with the measured counts. Thus in Sections 2.2.1 and 2.2.2, two new reconstruction approaches have been outlined, both of which are based on modeling the physics of the photon emission phenomenon. Both of these approaches seem to give a reasonably good reconstruction of the tracer location. The second approach (Section 2.2.2) also suggests that the phenomenon of buildup due to the presence of stainless steel column walls might be the cause for the large spread in the calibration curve (refer to Figure 2.2). This suggestion led us to explore a new data acquisition strategy, as outlined below.

3. A NEW DATA ACQUISITION STRATEGY

This strategy is based on the assumption that the observed scatter in the calibration curve is caused by buildup at the stainless steel column wall. Through Figures 2.10a and 2.10b, we also established that the presence of buildup affects only the Compton scattering portion of the energy spectrum and not the photopeak fraction of the spectrum. Hence the new data acquisition strategy was to acquire only the photopeak fraction of the energy spectrum and then examine the appearance of the calibration curve. These calibration experiments were performed in a stainless steel column (O.D.= 10.4 in (26.4 cm) and thickness = 0.24 in (0.6 cm)) surrounding an 8.5 in (21.6 cm) stirred tank reactor with the impeller rotating at 400 rpm (corresponding to tip speed of V_{tip}=1.4 m/s), with gas being sparged at 10.0 scfh. The resulting calibration curve is shown in Figure 3.1:

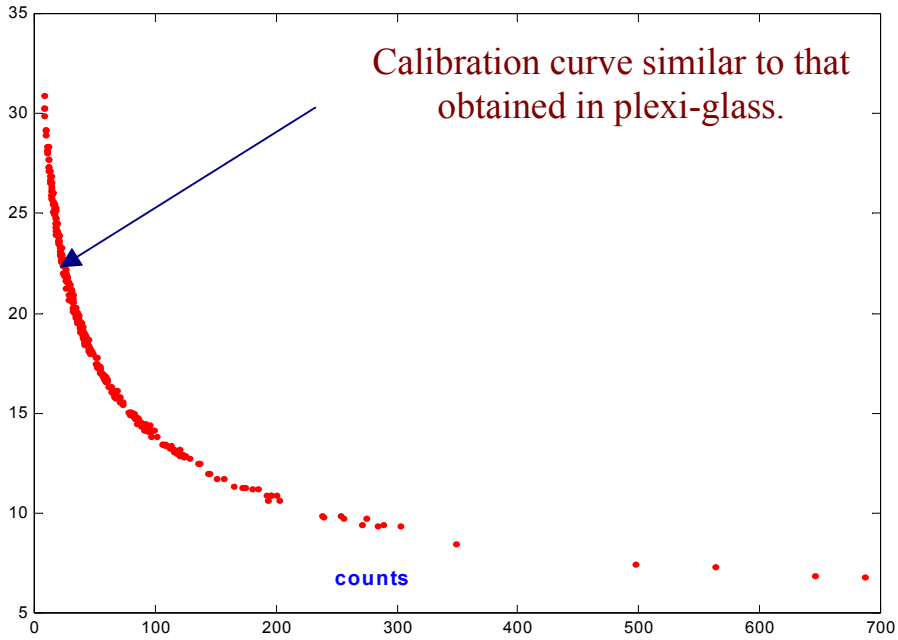

Figure 3.1 Calibration Curve Obtained in S.S. Column for Detector #1 by Acquiring Photopeak Fraction Alone

Figure 3.1 suggests that acquiring only the photopeak fraction of the energy spectrum results in a calibration curve that is very similar to the calibration curve obtained in the Plexiglas column (refer to Figure 2.1), with the only difference being the gradient of the calibration curve in the range of tracer to detector distances that are of interest. The gradient of the calibration curve depends on the attenuation coefficient of the intervening medium. In a stainless steel column, the gradient of the calibration curve is steeper than in a Plexiglas column due to the higher attenuation coefficient of the stainless steel column wall. The above calibration curve suggests that with this new data acquisition strategy, particle reconstruction should be reasonably accurate with the existing spline/weighted least squares regression approach. Hence, the time-averaged counts registered by each detector corresponding to the known calibration points were fed to the existing spline-based reconstruction approach. The details of reconstructing the 396 known calibration points are shown in Figures 3.2a and 3.2b. These figures suggest that the existing spline-based approach can reconstruct the known calibration points well, except for the calibration points near the bottom, top and walls of the column. The reconstruction is definitely much better than seen earlier (Figure 2.3).

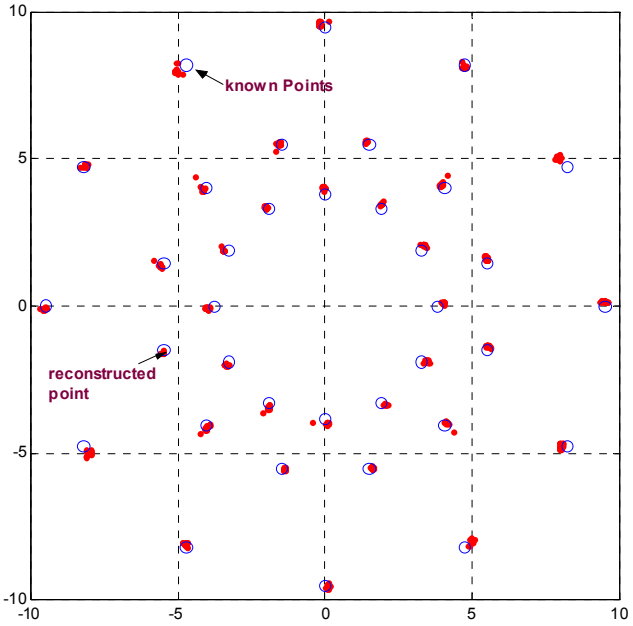

Figure 3.2a Reconstruction of 396 Known Calibration Points Projected onto a Horizontal Plane

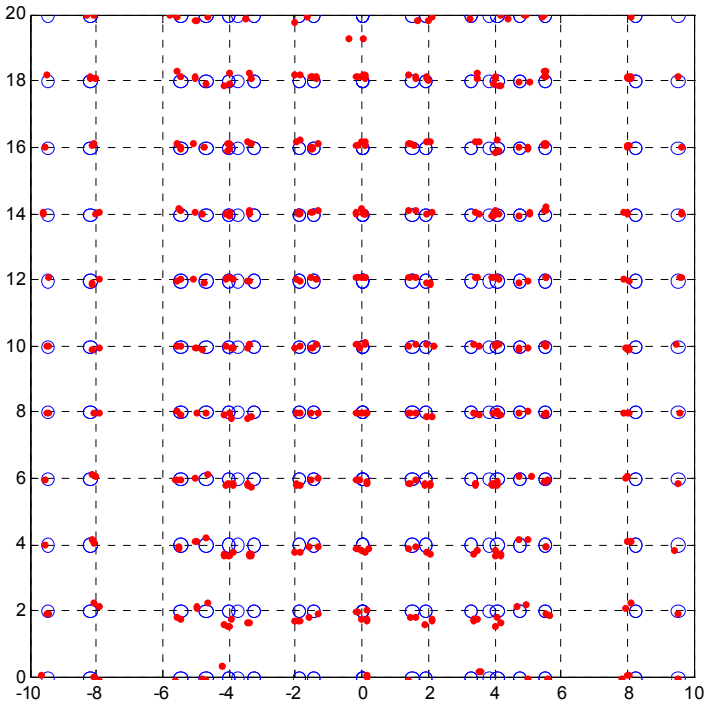

Figure 3.2b Reconstruction of 396 Known Calibration Points Projected onto an r-z Plane

In both Figures 3.2a and 3.2b the blue circles represent the known calibration points, while the red dots represent the reconstructed point. Further, the spline-based approach was used for reconstructing 36 test locations (corresponding to 3 radial locations 3.8, 5.7 and 9.5 cm, θ=0-360^o, z=0-20 cm, $\Delta\theta$=30^o and Δz=2.0 cm). The details of reconstructing a set of 12 test points corresponding to one axial plane (z=5.0 cm) are shown in Figure 3.3. The figure suggests that, corresponding to the 256 instantaneous samples acquired for each test point is a distribution in the reconstructed co-ordinate at that point. This distribution around each test point is not circular, but elliptical. However, the major axis of the ellipse is oriented in the same angular direction as the test point. The mean radial location of each distribution is 7.02 cm, suggesting that there is a negative bias in the reconstructed radial mean locations (i.e., underestimate in radial location). Since there is a bias in the estimated mean radial location, when variances are computed with respect to the real radial location (i.e., 7.2 cm) these do not converge with an increase in the number of samples. Hence the variances were computed around the reconstructed radial location. This σ_r is of the order of 4.0 mm, which is comparable to σ_r reported by Larachi et. al. (1994), that is, a radial σ_r of 2.5-3.0 mm when they acquired data at 33 Hz.

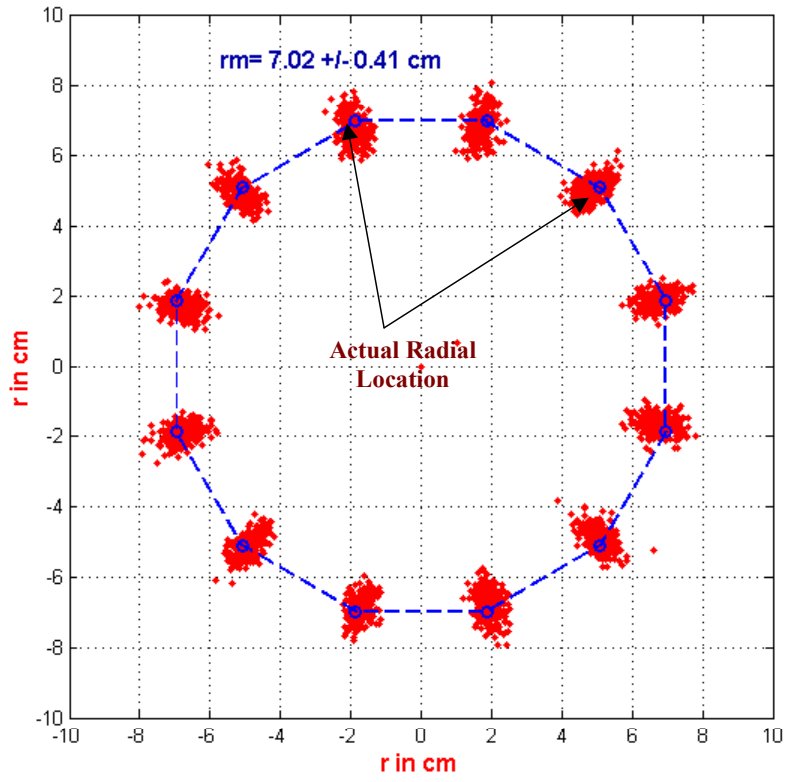

Figure 3.3 Details of Reconstructing 12 Test Points (r=7.2 cm, θ=15^o-345^o, z=5.0cm) from 3072 Instantaneous Samples Acquired at 50 Hz

They have also shown that the radial variance and the axial variance decrease with a decrease in sampling frequency and increase with an increase in sampling frequency. This variation from Larachi et. al.'s work (1994) is reproduced in Figure 3.4.

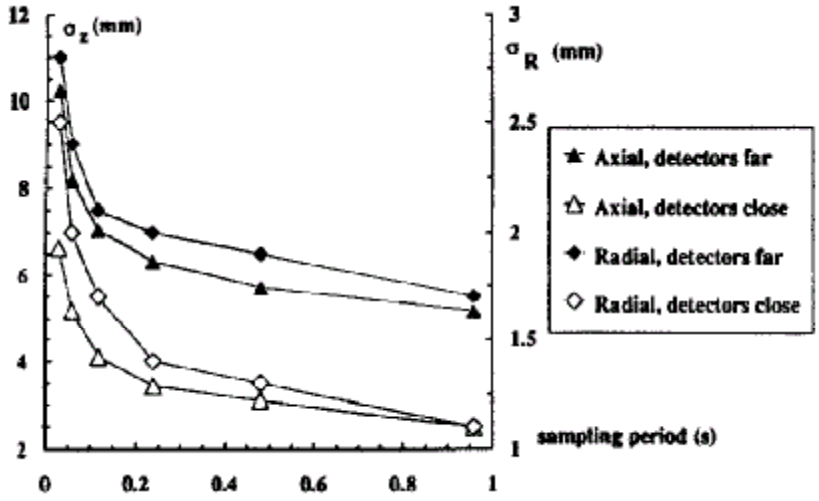

Figure 3.4 Variation in σ_r and σ_z with Sampling Frequency

However, it must be noted that while the variation in Figure 3.4 was obtained with 8 detectors, the current study used 16 detectors. Also Larachi et. al.'s (1994) experiments were conducted in a Plexiglas column with a tracer of strength 200μCi, while the current experiments were carried out in a stainless steel column with a tracer of strength 200μCi. Furthermore, Larachi et. al.'s column diameter was 4 inches, while the current setup diameter is 10.4 inches. Given all these differences, the radial σ_r obtained in the current study seems reasonable. The accuracy in reconstructing all the 36 test locations is summarized in Table 3.1.

Location	R_{actual} (cm)	R_{recon} +/- σ_r (cm)	Z_{actual} (cm)	Z_{recon} +/- σ_z (cm)
1	7.2	7.02 +/- 0.41	5.0	5.1 +/- 0.45
2	7.2	6.93 +/- 0.38	10.0	10.0 +/- 0.40
3	7.2	6.96 +/- 0.40	15.0	14.9 +/- 0.46

Table 3.1 Summary of Reconstruction Accuracy of 36 Test Locations (1 radial location, 3 axial locations and 12 angular locations)

Table 3.1 suggests that the estimate of the mean radial location as well as the mean axial location is biased. The radial estimate is always negatively biased, while the axial estimate is positively biased in the center of the column, but towards the top it is negatively biased. The σ_r and σ_z are all comparable and are between 4.0-4.5 mm. These numbers are comparable to similar values reported by Larachi et. al. (1994). On the face of it, the σ_z (4.0-4.5 mm) from the current study may seem to be better than those of Larachi et. al. (9.5 –11.0 mm). However, it must be kept in mind that Larachi et. al.'s study used only 8 detectors, while in the current study 16 detectors were used. In order to analyze the effect of detector configuration and number of detectors, the above analysis was repeated for two different detector configurations. In the first detector configuration only 8 detectors were used, as shown in Figure 3.5:

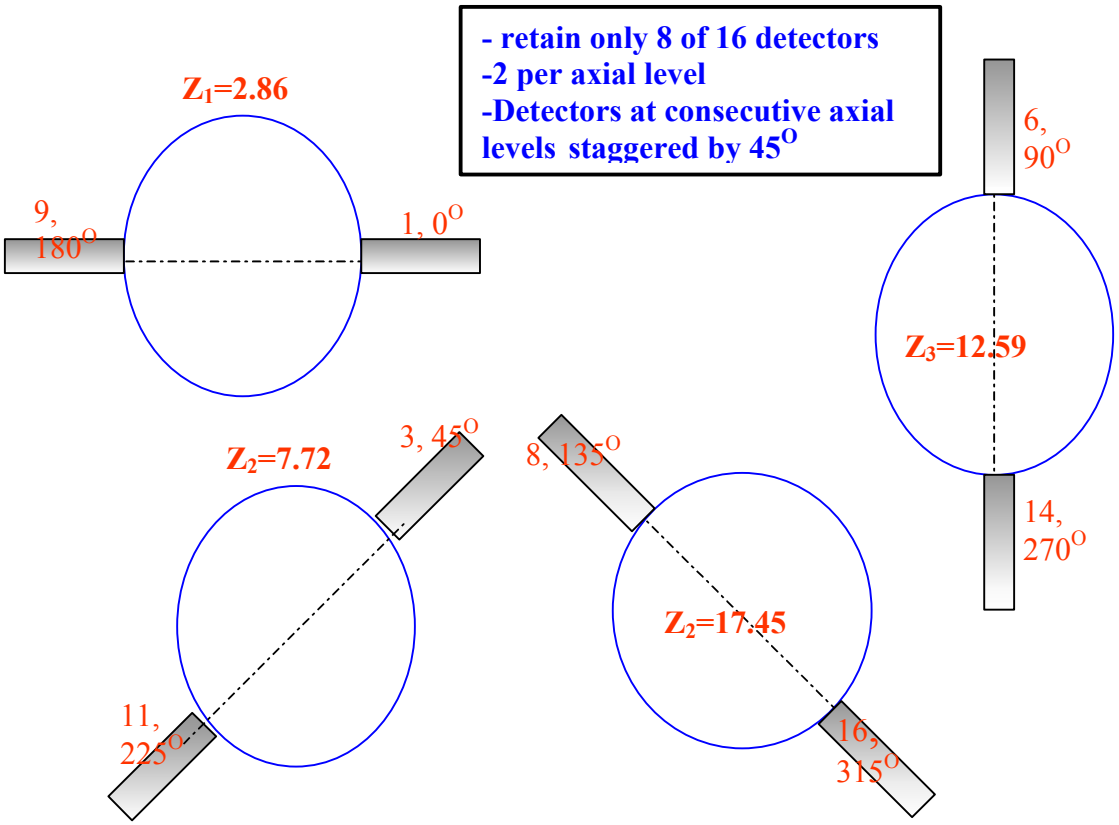

Figure3.5 Analysis of Effect of Detector Configuration on Reconstruction Accuracy

The accuracy in reconstructing the 36 test points after hiding 8 detectors is reported in Table 3.2.

Location	R_{actual} (cm)	R_{recon} +/- σ_r (cm)	Z_{actual} (cm)	Z_{recon} +/- σ_z (cm)
1	7.2	7.08 +/- 0.69	5.0	5.31 +/- 1.29
2	7.2	7.05 +/- 0.65	10.0	9.92 +/- 1.11
3	7.2	7.00 +/- 0.73	15.0	14.22 +/- 1.44

Table 3.2 Summary of Reconstruction Accuracy of 36 Test Locations (1 radial location, 3 axial locations and 12 angular locations) after not including 8 Locations

Table 3.2 suggests that by not including 8 detectors in the analysis, the error in the estimate of the mean axial location has increased. The σ_r and σ_z have also increased, with $\sigma_r(8)/\sigma_r(16)\sim1.75$ and $\sigma_z(8)/\sigma_z(16)\sim3.0$. The σ_z appears large (11-14 mms), but is comparable to the values reported by Larachi et al. with 8 detectors. Hence Table 3.2 suggests that the number of detectors used for reconstruction definitely affects the reconstruction accuracy. This was also the case when only 4 detectors were used for reconstruction. These results are summarized in Figures 3.6a and 3.6b, respectively.

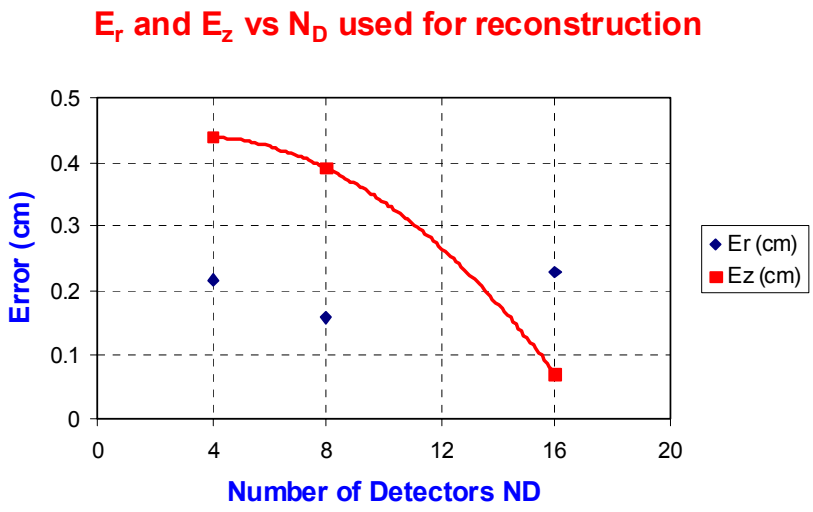

Figure 3.6a Variation of Radial and Axial Bias with Number of Detectors used for Reconstruction

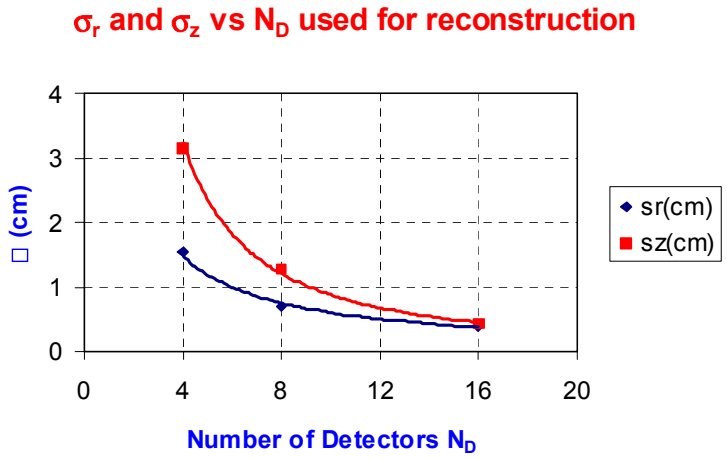

Figure 3.6b Variation of σ_r and σ_z with Number of Detectors used for Reconstruction

Figure 3.6a suggests that the bias in the radial estimate is little affected by the number of detectors used for reconstruction, while the bias in the axial estimate decreases with an increase in the number of detectors (4.0 to 0.5 mm). Figure 3.6b suggests that σ_z is comparable to σ_r for a large number of detectors, and σ_z and σ_r progressively increase as the number of detectors decreases. The rate at which σ_z increases is higher than the rate at which σ_r increases. This suggests that the error boundaries associated with the particle position reconstruction change from a sphere (when N is large) to an ellipsoid (when N is small). To generalize these results, one would need to look at the variation of σ_r and σ_z with detector density (defined as N_D/(Active volume of interest in reactor)). The above analysis suggests that with the new data acquisition strategy, even the existing spline-based/weighted regression technique can be used to obtain reasonably good estimates of the tracer location in the stainless steel column. Hence this approach will be used for the time being for analysis of CARPT experiments performed in the High Pressure Bubble Column reactor at the conditions of interest.

Future Work

Future work planned for Washington University includes the three-dimensional simulation of two-phase flows (air and water) in bubble columns, using CFDLIB.

References

Devanathan, N., Investigation of liquid hydrodynamics in bubble columns via computer automated radioactive particle tracking (CARPT), D.Sc., Saint Louis, Missouri (1991).

Larachi, F., G. Kenedy and J. Chaouki, A γ-ray detection system for 3-D particle tracking in multiphase reactors, *Nucl. Instr. and Meth.*, **A338**, pp.568-576 (1994).

Roy, S., F. Larachi,, M.P. Dudukovic', R. Dodson, and M.H. Al-Dahhan, Implementation of computer automated radioactive particle tracking (CARPT) on a gas-solid riser: experiment design and analysis, CREL Internal Report (1999).

Tsoulfanidis, N., Measurement and detection of radiation, McGraw Hill, New York (1983).

IOWA STATE UNIVERSITY

The report from Iowa State University for the period follows.

CFD INVESTIGATION OF SLURRY BUBBLE COLUMN HYDRODYNAMICS

Fifth Quarterly Report

Reporting Period: October 1 – December 31, 2000)

Highlights

- Determined the domain size necessary to represent all the flow scales in a gas-liquid bubble column at high superficial gas velocity.
- Ported CFDLIB and conducted scaleup studies on the INTEL LINUX cluster at the Scalable Computing Laboratory, Ames Laboratory.
- Ported the parallel version of CFDLIB code to the SGi Origin 2000 at the ISU high-performance computing facility.
- Ran simulations using periodic boundary conditions for the largest domain size in order to study the hydrodynamics of a wide-diameter gas-liquid bubble column.

Summary of Progress

First, air-water bubble column simulations were performed for different grid sizes and domain sizes. An analysis of the spectra for these simulations led to the determination of the minimum domain size needed to represent all significant flow structures within the column width. Currently we are conducting simulations for a 256-cm wide column with different grid sizes.

All of our earlier simulations utilized the sequential version of CFDLIB code. At this time we have implemented a parallel version of the code, investigated periodic boundary conditions, and performed scaleup studies. The parallel version of the code cannot as yet handle periodic boundary conditions on distributed memory (cluster) computers. We are working with consultants at the ISU high-performance computing center to modify the code to correct this problem.

We plan to acquire an Alpha cluster machine for our research group during the first or second quarter of 2001. As a means of preparation, scaleup studies on the Ames Laboratory Intel Cluster were performed for three-dimensional simulations. The dimensions of the bubble column were chosen as the largest problem that can be solved using one node of the cluster. This smaller problem does not show any increase in speed of solution with a higher number of processors. Similar studies will be performed on the Ames Laboratory Alpha Cluster using the periodic boundary condition code after it has been modified for parallel machines.

Simulation Results

This section summarizes the simulation results obtained during the fourth quarter of 2000 for a two-dimensional air-water bubble column. In all cases, the air was introduced uniformly into the bottom of the column with a superficial air inlet velocity of 12 cm/sec. Grid and domain sizes for each case are listed in Table 1. The simulations were allowed to attain a statistical steady state before data were collected for time averaging.

Table 1 Description of Grid Size and Domain Size for Different Simulation Cases

Simulation case	Grid size (cm X cm)	Domain size (width X height)	Simulation time for calculation of time-averaged quantities (seconds)
1	1 X 1	**64 X 128**	50
2	2 X 2	64 X 128	72
3	2 X 2	128 X 128	150
4	4 X 4	**128 X 128**	20
5	2 X 2	**256 X 256**	20

Figure 1.1 illustrates the profile of kinetic energy of the water phase with respect to time for three different domain sizes. As shown in this figure, the largest domain size (256 X 256) displays a maximum of approximately 4500 cm^2/sec^2 at approximately 20 seconds. (The computational cost of running this simulation on a single-processor machine prohibited us from continuing the calculation beyond 20 secs.) The 128X128 domain exhibits a maximum of nearly 5000 cm^2/sec^2 at a time of 100 seconds. However, statistically its behavior is very similar to that of the largest domain. For the smallest domain size (64 X 128), the kinetic energy tended to increase with time throughout the 150-second period observed, and exhibited much smaller fluctuations. The value at the end of the run was very similar to the other cases. The lower fluctuation levels were undoubtedly due to low-pass filtering of the velocity fields by the "coarse" computational grid.

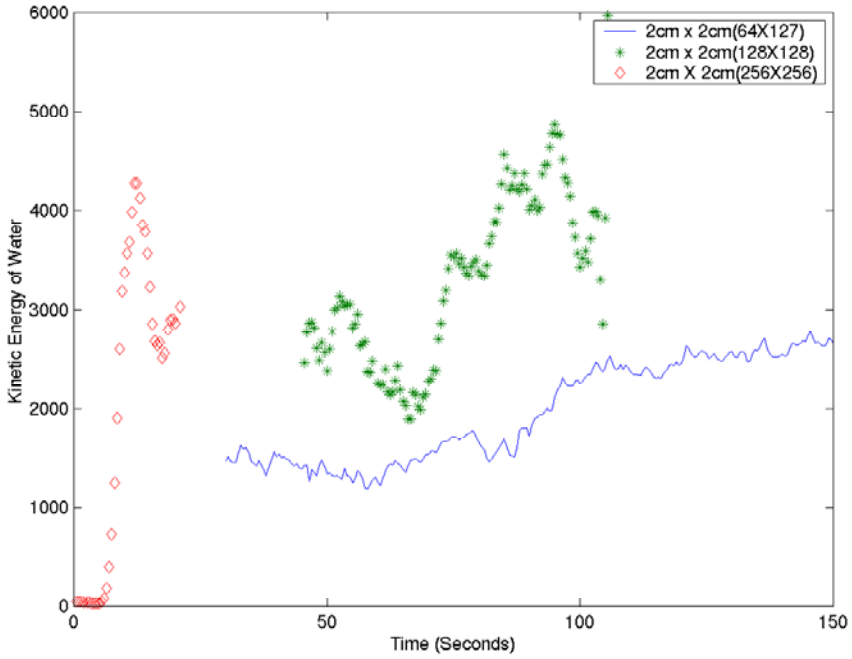

Figure 1.1 Sample Kinetic Energy (cm^2/sec^2) Time Series in Water Phase for Three Different Domain Sizes

Figures 1.2 and 1.3 show the spectra of water velocity components for four different cases. The abrupt decrease at the Nyquist frequency [defined as 1/(2*sampling interval)] signifies that the (molecular) viscous dissipation term of the multi-component momentum equations are not resolved for these flows. This cut-off implies that we are essentially neglecting the viscous dissipation term. The simulations are then essentially *inviscid* two-phase flow (with grid spacing greater than or equal to 1 cm) and rely on the low-pass filtering property of the grid to dissipate energy (i.e., crude LES). Since most CFD studies that have appeared in the literature have used a grid size on the order of 1 cm for the air-water system, these must also suffer from under-resolution. It can also be observed in Figure 1.2 that the total energy of the spectra increases with increasing resolution. Note also in Figure 1.3 that the vertical velocity component (v) is slightly more energetic than the horizontal component, as would be expected due to the vertical drag force. Similar (and perhaps even stronger) anisotropy has been observed in the bubble-column experiments of Zenit, et. al. (2000). We plan to explore this question further by performing simulations of the Zenit experiment in the coming year.

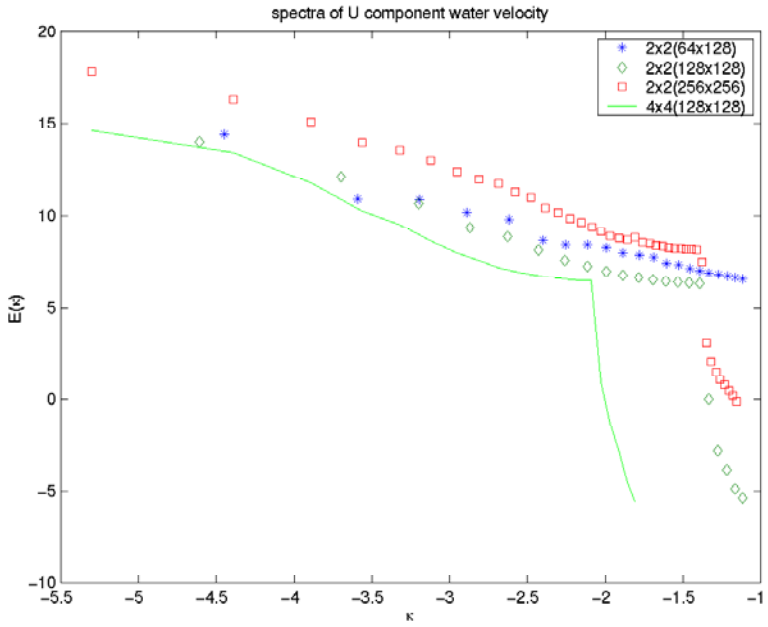

Figure 1.2 Spectra of U Component of Water Velocity for Four Different Cases

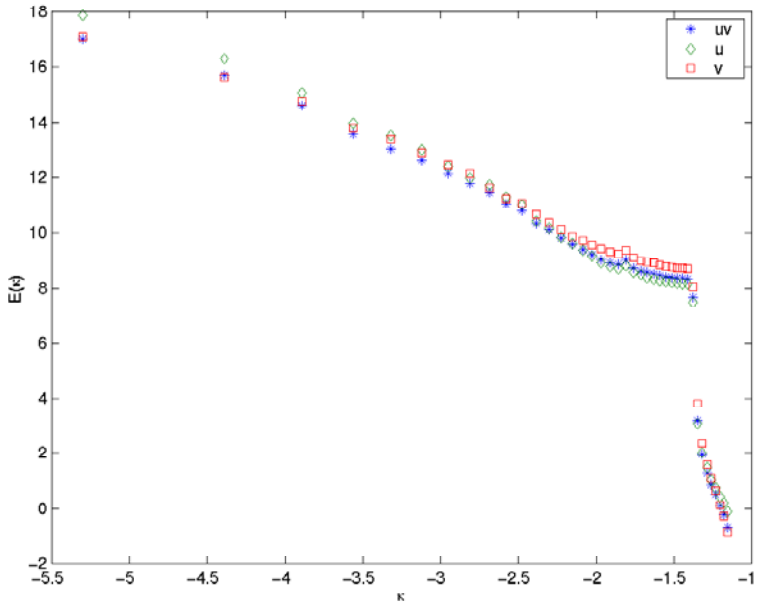

Figure 1.3 Spectra of u, v and Cross Term of Water-Phase Velocity for Case 5
LINUX Cluster Scaleup Study

The computational cost associated with three-dimensional, high-resolution simulations has led us to port CFDLIB to parallel hardware. In order to test the computational gains that are achievable using multiple processors, a scaleup study was performed on the Ames Laboratory INTEL cluster. For this study, the following column parameters were used:

Length = 50 cm Height = 160 cm

Width = 50 cm Grid Spacing = 1 cm

In addition, it was assumed that air was introduced uniformly to the column at a rate of 8 cm/sec. The average time taken per iteration is shown in Table 2 and Figure 2.1.

Table 2 Average Time per Iteration taken by CFDLIB on INTEL LINUX Cluster for Different Numbers of Processors

Number of Processors Used	Average time per iteration (in minutes)
1	2.83
3	2.07
4	1.92
5	1.45
8	1.02

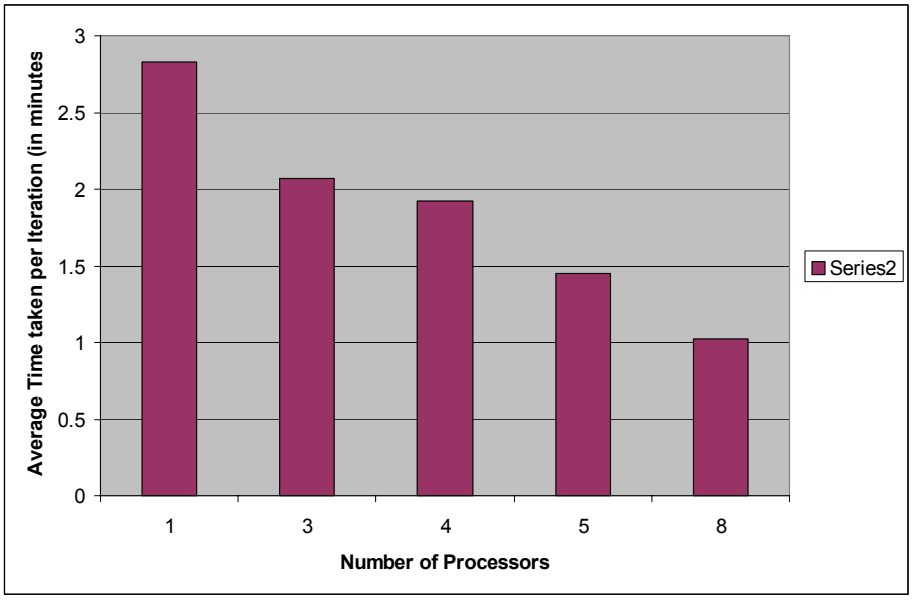

Figure 2.1 Average Time (minutes) per Iteration for Various Numbers of Processors

As shown in Table 2 and Figure 2.1, using eight processors improves the speed by a factor of 2.24 over the use of a single processor, which is reasonable when compared to the ideal speed-up factor of 4. Since CFDLIB is a block-structured code, the time taken per iteration should halve on doubling the number of processors. From this study, it appears that going beyond eight processors may improve the performance, but the gains will be modest. It was also discovered in the process of running these simulations that the parallel version of the code with periodic boundary conditions yields incorrect answers. We are thus looking into the cause of this problem with the help of the consultants at the ISU High-Performance Computing group. The next step in the parallelization study will be to port the code to the Ames Laboratory Alpha cluster. The single-processor speed of the Alpha is 4-5 times faster than the SGi Origin. This increase in performance should yield better scaleup characteristics on the Alpha cluster than the Intel cluster for large problems. We plan to purchase an Alpha cluster for our research group in the first quarter of 2001.

Future Work

Iowa State will next study free-slip boundary conditions versus periodic boundary conditions to determine whether or not free-slip boundary conditions could be a suitable alternative. Also, CFDLIB will be used to simulate conditions described in Zenit et al.

References

Zenit, R., D.L. Koch, and A.S. Sangani, Measurements of the average properties of a suspension of bubbles rising in a vertical channel, *J. Fluid Mech.* Vol. 420, pp.1-36 (2000).

OHIO STATE UNIVERSITY

The report from Ohio State for the period follows.

INTRINSIC FLOW BEHAVIOR IN A SLURRY BUBBLE COLUMN UNDER HIGH PRESSURE AND HIGH TEMPERATURE CONDITIONS

Quarterly Report

(**Reporting Period:** October 1 to December 31, 2000)

Highlights

- The study of gas injection phenomena from a submerged single orifice in liquid-solid suspensions at high pressures has been completed. The effects of pressure and solids concentration on the bubbling-jetting transition velocity have been investigated.

- The bubbling-jetting transition velocity decreases with increasing pressure, and increases with the presence of particles.

- The study of flow fields and Reynolds stresses at high pressures using a two-dimensional laser Doppler velocimetry (LDV) system has been initiated. Experiments are currently being conducted in the 2-inch high-pressure vessel.

- The study of axial liquid-phase mixing at high pressures has been initiated. Previous studies on liquid-phase mixing at elevated pressures and measurement techniques were reviewed.

Work Conducted

1. Study of Bubbling-Jetting Transition

The effects of pressure and particle presence on the bubbling-jetting transition velocity from a single orifice connected to a gas chamber were studied. Figure 1 shows the effects of pressure and solids concentration on the transition velocity from the bubbling to jetting regimes. For both the liquid and the liquid-solid suspension, when pressure or gas density increases, the bubbling-jetting transition velocity decreases significantly, especially in the low-pressure range. At very high pressures, the decrease in the transition velocity with increasing pressure is relatively small. The acceleration of the transition to the jetting regime at high pressures is mainly due to an increase in the gas momentum. Based on the experimental data, it was found that the effect of pressure on the transition velocity can be expressed by the following relationship:

$$u_{jetting} \propto \rho_g^{-n} \tag{1}$$

where the index n is a function of the solids concentration. For the system used in this study, n varied from 0.3 for liquids to 0.4~0.5 for liquid-solid suspensions.

The effect of particle presence on transition velocity is also provided in Figure 1, which shows that the particle effect strongly depends on the pressure. In the low-pressure range (P<2.5MPa), the effect of particles on the transition velocity is significant. The presence of particles increases the transition gas velocity significantly. For example, at atmospheric pressure, the transition velocity in the liquid is about 7.0 m/s. When the solids concentration increases to 0.18 vol %, the transition velocity increases from 7.0 to 12.0 m/s (71% increase). In the high-pressure range (P>2.5MPa), the effect of solids concentration on the transition velocity is insignificant.

The effect of pressure on the critical mass flux of gas is shown in Figure 2. The critical mass flux of gas is defined as the mass flux of gas at the transition point, *i.e.*, equal to $\rho_g u_{jetting}$. It can be seen that the critical mass flux of gas is not constant and increases with an increase in pressure. At very high pressures (P>10 MPa), the critical mass flux of gas tends to approach a constant value.

The effects of pressure and solids concentration on the critical Weber number, defined as the Weber number at the transition point, We_{cr} ($=\frac{\rho_g u_{jetting}^2 D_0}{\sigma}$), are shown in Figure 3. For bubbling-jetting transition in liquids, the critical Weber number increases significantly with an increase in pressure, which is possibly due to the increased liquid viscosity with pressure. Rabiger and Vogelpohl (1982) also found that the critical Weber number increases with an increase in liquid viscosity. At atmospheric pressure, the critical Weber number is about 3 for the present liquid system, while at high pressures (*e.g.*, P=8.3 MPa), the critical Weber number is above 10. With an increase in solids concentration, the difference in the critical Weber number among various pressures becomes smaller. As shown in the figure, when the solids concentration reaches 30 vol %, the critical Weber number is almost constant over the pressure range studied. The effect of solids concentration on the critical Weber number is insignificant at high pressures.

2. Study of Flow Fields and Reynolds Stresses

In order to achieve better penetration of laser beams, new pairs of quartz windows and spacers were installed in the 2-inch, high-pressure column. The test and calibration of the LDV system were completed, and the measurements of liquid velocity profiles at high pressures are currently being conducted in the 2-inch vessel. Some preliminary results will be reported in the next quarter.

3. Study of Axial Liquid-Phase Mixing

Literature Review

Liquid-phase mixing is an important parameter in the design of industrial reactors. The liquid-phase mixing strongly depends on the hydrodynamics and bubble characteristics. Previous studies have shown that pressure has significant effects on gas holdup, bubble size and bubble rising velocity. Therefore, the study of pressure effect on liquid-phase mixing is necessary to further understand flow behaviors in bubble columns and slurry bubble columns.

The studies regarding the axial liquid-phase mixing in gas-liquid systems at atmospheric conditions are extensive, especially for the air-water system; however, studies under high-pressure conditions are very scarce. Houzelot et al. (1985) measured the axial dispersion of the liquid phase in a bubble column with a diameter of 5 cm. They found that pressure did not affect axial dispersion, which was limited by the narrow experimental conditions in their study, *i.e.*, very low superficial gas velocity (<6 mm/s) and pressure (< 3 atm). Under very low gas velocities, the flow was always in the homogeneous bubbling regime, and a significant change in liquid-phase mixing was not expected. Sancnimnuan et al. (1984) experimentally investigated the extent of liquid-phase backmixing under coal hydroliquefaction conditions (*e.g.*, temperature between 164 and 384^{0}C and pressure between 4.5 and 15 MPa) in a small bubble column reactor (1.9 cm in diameter). They did not describe the effect of pressure on axial mixing, and their study was limited by the small scale of the reactor.

Holcombe et al. (1983) determined the liquid axial-dispersion coefficient in a 7.8-cm diameter bubble column under pressures in the range of 3.0~7.1 atm. The superficial gas velocity varied up to 0.6 m/s. They used heat as a tracer to measure the thermal dispersion coefficient, which was found to be comparable to the mass dispersion coefficient. In their study, the effect of pressure on thermal dispersion coefficients was negligible. Wilkinson et al. (1993) measured the liquid axial-dispersion coefficient in a batch-type bubble column of 0.158-m diameter for the water-nitrogen system at pressures between 0.1 and 1.5 MPa using the electrical conductivity cell. They found that the liquid axial-dispersion coefficient actually increased with increasing pressure, especially under high gas velocity (> 0.10 m/s). They also found that the available theories in the literature describing liquid mixing under atmospheric pressure could not explain the pressure effect observed in their study. They proposed a procedure to estimate the liquid-phase dispersion coefficient at elevated pressures based on liquid holdup and the dispersion coefficient at ambient pressure, *i.e.*,

$$E_l(\text{high pressure}) = E_l(\text{atmospheric}) \cdot \frac{\varepsilon_l(\text{atmospheric})}{\varepsilon_l(\text{high pressure})}. \tag{2}$$

Wilkinson et al.'s 1993 study was also limited by the narrow experimental conditions (low pressure) and limited batch system (air-water), and their conclusion on the pressure effect and the proposed correlation need to be further verified. Tarmy et al. (1984) used radioactive tracers to study the liquid back-mixing in pilot coal liquefaction reactors. They found that the measured dispersion coefficients at high pressures (17 MPa) were up to 2.5 times smaller than the predictions by literature correlations, which usually were proposed for ambient conditions in air-water systems. However, they did not present their mixing data in the paper. The detailed

information of high-pressure studies available in the literature regarding liquid-phase mixing in bubble columns is shown in Table 1.

Objective of Study

Although some research has studied the effect of pressure on liquid mixing in bubble columns, those studies were confined to low gas velocities or low pressures (less than 1.5 MPa), small column sizes and limited systems (air-water). Furthermore, the effect of pressure effect was still not conclusive. Further systematic studies are needed to cover a wide range of operating conditions and should be conducted in systems close to industrial applications. The objective of this study is to develop the suitable measurement technique to investigate axial liquid-phase mixing in a hydrocarbon liquid at high pressures.

Measurement Technique

Axial mixing of the liquid phase is normally described by a one-dimensional dispersion model. The dispersion coefficient can be determined by unsteady and steady tracer injection methods. It has been verified that both measurement principles lead to the same results (Deckwer et al., 1974). In the steady injection method, a tracer is injected at the exit or some other convenient point, and the concentration profile is obtained by sampling upstream. With the unsteady injection method, a variable flow of tracer is injected, usually at the contactor inlet, and samples are normally taken at the exit. The most common form of injection is the single impulse, and the response of the tracer input is then obtained at the sampling point. Other forms of injection are the step change, oscillatory and random forms. The tracer for both the steady and unsteady tracer injection methods can be an electrolyte, a dye or heat. The mass dispersion method normally uses electrolyte as the tracer, and the change in electrical conductivity is measured. This method is only suitable for aqueous liquids. The thermal dispersion method uses heat as the tracer, and the temperature distribution within the column is measured. This method can also be applied to non-aqueous liquids, for example, hydrocarbon liquids. The thermal dispersion method is thought to give more accurate results than the mass dispersion method, because the experimental operation is easily achieved for the former.

In this study, because the liquid used was hydrocarbon liquid, the thermal dispersion method was chosen to study the axial liquid-phase mixing. The axial dispersion coefficients of the liquid phase were measured by the steady-state thermal dispersion method, *i.e.*, introducing heat close to the outlet of the liquid phase and measuring the upstream temperature profile in the liquid when the temperature distribution reached steady state. The schematic of typical axial temperature distribution across the column is shown in Figure 4. The dispersion coefficient can be determined from the temperature profile based on the one-dimensional dispersion model. Since the heat capacity of gas is much smaller than that of liquid, the temperature change in the column is mainly due to the backmixing of liquid. Considering that the heat losses through the column wall and the gas-liquid interface are negligible, the following differential energy balance equation applies (Aoyama et al., 1968; Wendt et al., 1984):

$$\frac{k_l}{\rho_l C_{pl}} \frac{d^2T}{dz^2} + \frac{U_l}{1-\varepsilon_g} \frac{dT}{dz} = 0 \qquad \text{with } E_l \equiv \frac{k_l}{\rho_l C_{pl}} \tag{3}$$

where E_l is the effective thermal dispersion coefficient and is comparable to the mass dispersion coefficient, z is the axial position from the liquid outlet and $z=0$ represents the liquid outlet. This differential equation can be solved analytically after the boundary conditions for a semi-infinite reactor are introduced, *i.e.*,

$$\begin{aligned} T &= T_m \quad \text{at } z = 0 \\ T &= T_0 \quad \text{at } z = \infty \end{aligned}, \tag{4}$$

where T_0 and T_m are the inlet and outlet liquid temperatures, respectively. T is the liquid temperature at distance z from the liquid outlet. The analytical solution of the differential equation is:

$$\ln \frac{T - T_0}{T_m - T_0} = -\frac{U_l}{E_l\left(1-\varepsilon_g\right)} z \tag{5}$$

Equation (5) indicates that the relationship between $ln[(T-T_0)/(T_m-T_0)]$ and z is linear, and the dispersion coefficient, E_l,, can be calculated from the slope of the temperature distribution curve, provided that the dispersion coefficient is constant and the gas holdup and superficial liquid velocity are known. It was proven that dispersion coefficients measured by mass and thermal methods are comparable, as shown in Figure 5 (Wendt et al., 1984). The validity of the thermal dispersion technique was also verified by other researchers (Aoyama et al., 1968; Holcombe et al., 1983).

Future Work

The axial dispersion coefficients of the liquid phase will be measured by the steady-state thermal dispersion method. The study of flow fields and Reynolds stresses at high pressures using a two-dimensional laser Doppler velocimetry (LDV) system will be undertaken.

Notations

C_{pl}	heat capacity of liquid, J/(kg·^{0}C)
D_0	orifice diameter, m
E_l	liquid-phase dispersion coefficient, m^2/s
k_l	thermal conductivity of liquid, W/(m·^{0}C)
P	system pressure, Pa
T	temperature at axial position z, ^{0}C
T_0	liquid inlet temperature, ^{0}C
T_m	liquid outlet temperature, ^{0}C
u_0	superficial orifice gas velocity, m/s
$u_{jetting}$	bubbling-jetting transition velocity, m/s
U_l	superficial liquid velocity, m/s
V_c	gas chamber volume, m^3

We Weber number, $\frac{\rho_g u_0^2 D_0}{\sigma}$, dimensionless

Z axial height from the gas-liquid outlet, m

ε_g gas holdup, dimensionless

ε_l liquid holdup, dimensionless

ε_s solids concentration, dimensionless

ρ_g gas density, kg/m^3

ρ_l liquid density, kg/m^3

σ surface tension, N/m

References

Aoyama, Y., K. Ogushi, K. Koide, and H. Kubota, "Liquid mixing in concurrent bubble columns," *J. Chem. Eng. Japan*, **1**, 158 (1968).

Deckwer, W. D., R. Burckhart, and G. Zoll, "Mixing and mass transfer in tall bubble columns," *Chem. Eng. Sci.*, **29**, 2177 (1974).

Holcombe, N. T., D. S. Smith, H. N. Knickle, and W. O'Dowd, "Thermal dispersion and heat transfer in nonisothermal bubble columns," *Chem. Eng. Commun.*, **21**, 135 (1983).

Houzelot, J. L., M. F. Thiebaut, J. C. Charpentier, and J. Schiber, "Contribution to the hydrodynamic study of bubble columns," *Int. Chem. Eng.*, **25**, 645 (1985).

Rabiger, N., and A. Vogelpohl, "Bubble formation in stagnant and flowing newtonian liquids," *Ger. Chem. Eng.*, **5**, 314 (1982).

Sangnimnuan, A., G. N. Prasad, and J. B. Agnew, "Gas holdup and backmixing in a bubble-column reactor under coal-hydroliquefaction conditions," *Chem. Eng. Commun.*, **25**, 193 (1984).

Tarmy, B., M. Chang, C. Coulaloglou, and P. Ponzi, "Hydrodynamic characteristics of three phase reactors," *The Chemical Engineer*, October (1984).

Wendt, R., A. Steiff, and P. M. Weinspach, "Liquid phase dispersion in bubble columns," *Ger. Chem. Eng.*, **7**, 267 (1984).

Wilkinson, P. M., H. Haringa, and F. P. A. Stokman, "Liquid mixing in a bubble column under pressure," *Chem. Eng. Sci.*, **48**, 1785 (1993).

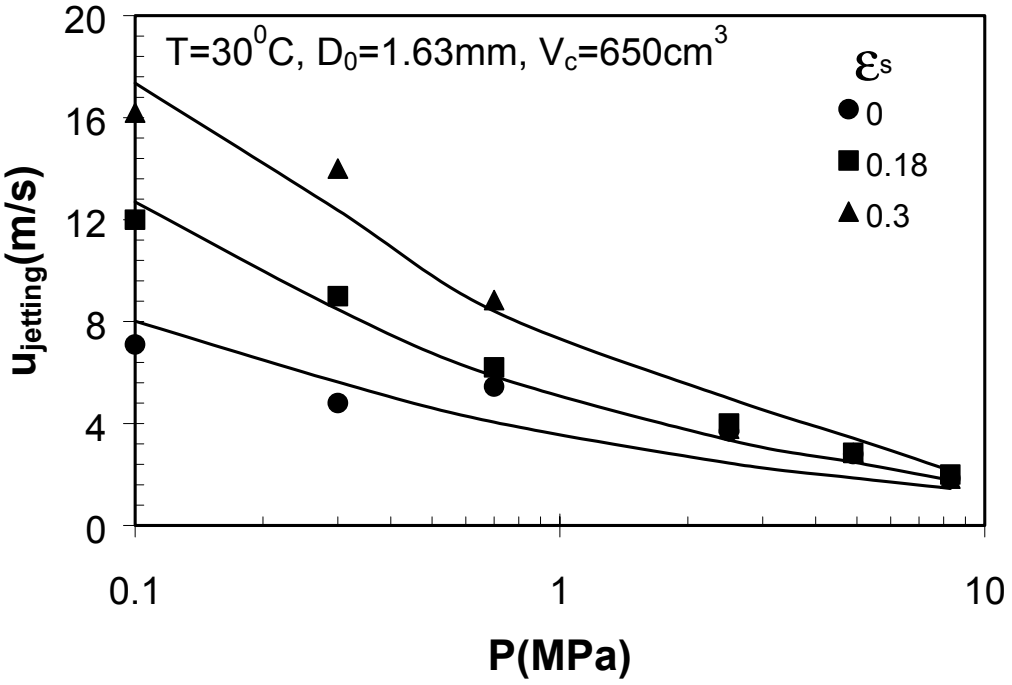

Figure 1 Effects of Pressure and Solids Concentration on Bubbling-Jetting Transition Velocity

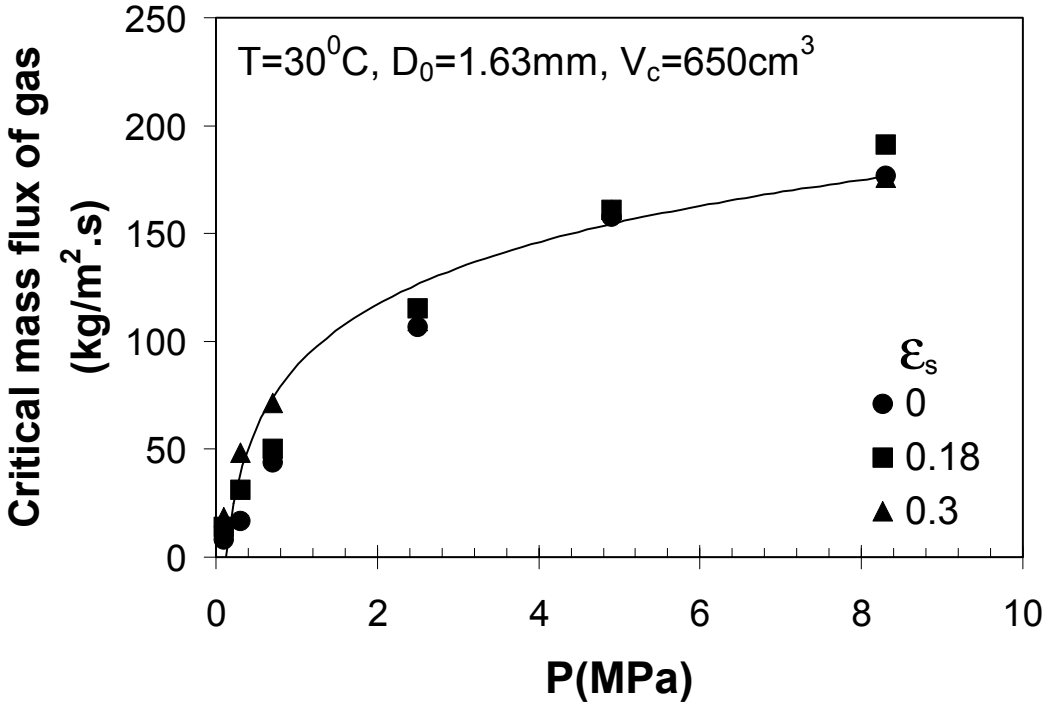

Figure 2 Effect of Pressure on the Critical Mass Flux of Gas Through the Orifice in Liquid and Liquid-Solid Suspensions

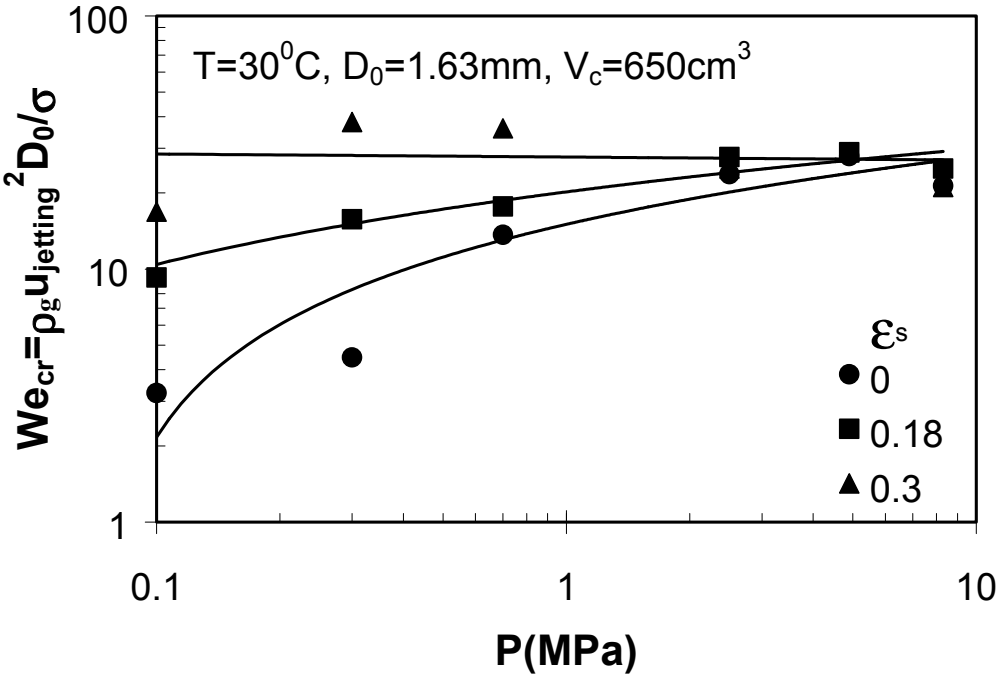

Figure 3 Critical Weber Number as a Function of Pressure and Solids Concentration

Table 1 Available High-Pressure Studies in the Literature Regarding Liquid-Phase Mixing in Bubble Columns

Reference	Technique	System	D (cm)	P (MPa)	U_g (cm/s)	U_l (cm/s)	Pressure effect
Holcombe et al. (1983)	thermal	N_2-water	7.8	0.3~0.7	0~60	0~2.0	insignificant
Sancnimnuan et al. (1984)	mass	N_2-tetralin	1.9	4.5~15	0.2~1.1	0.1~0.3	insignificant
Houzelot et al. (1985)	mass	N_2-water	5.0	0.3	0.25~0.6	0.025~0.1	insignificant
Wilkinson et al. (1993)	mass	N_2-water	15.8	0.1~1.5	0~20	batch	increase
Tarmy et al. (1984)	mass (radioactive tracer)	H_2-hydrocarbon-coal	2.4 6.6 61	17	0.6~6.5	0.15~1.6	decrease

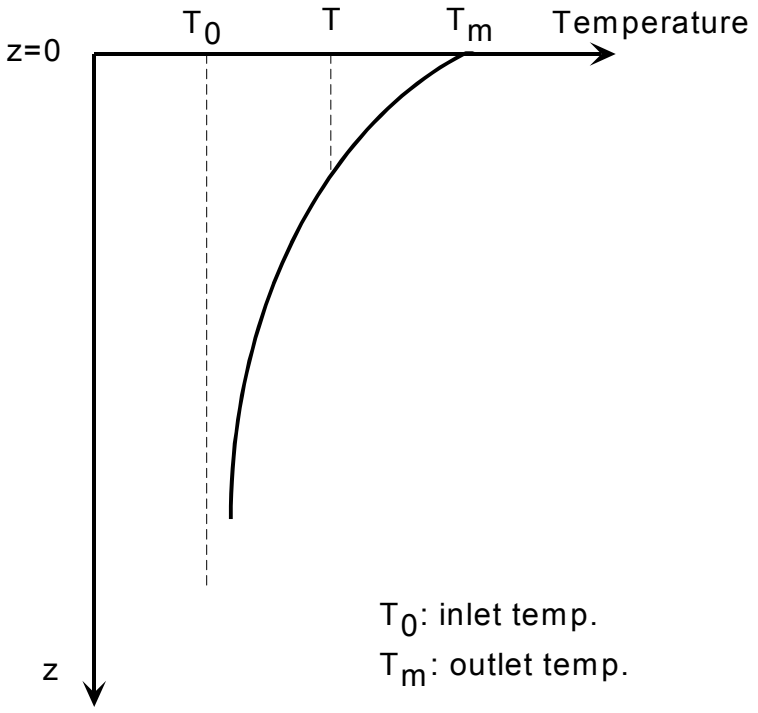

Figure 4 Typical Axial Temperature Distribution for Steady-State Thermal Dispersion Method

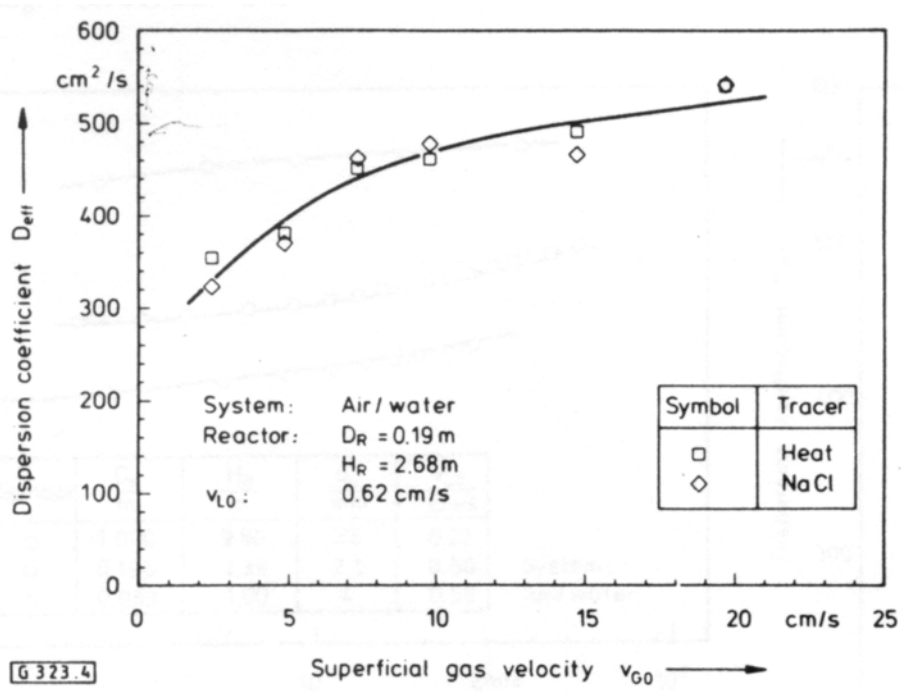

Figure 5 Comparison of Dispersion Coefficients Measured by Mass and Thermal Methods (Wendt et al., 1984)